In-Situ observation of New Particle Formation (NPF) in the tropical tropopause layer of the 2017 Asian Monsoon Anticyclone: Part II - NPF inside ice clouds

Ralf Weigel[1], Christoph Mahnke[2,6], Manuel Baumgartner[1,3], Martina Krämer[1,4], Peter Spichtinger[1], Nicole Spelten[4], Armin Afchine[4], Christian Rolf[4], Silvia Viciani[5], Francesco D'Amato[5], Holger Tost[1], and Stephan Borrmann[1,2]

[1]Institut für Physik der Atmosphäre, Johannes Gutenberg Universität, Mainz, Germany

[2]Partikelchemie, Max-Planck-Institut für Chemie, Mainz, Germany

[3]Zentrum für Datenverarbeitung, Johannes Gutenberg University, Mainz, Germany

[4]Institute of Energy and Climate Research (IEK-7), Forschungszentrum Jülich, Jülich, Germany

[5]National Institute of Optics - National Research Council (CNR-INO), Florence, Italy

[6]now at the Institute of Energy and Climate Research (IEK-8), Forschungszentrum Jülich, Jülich, Germany

Abstract

From 27 July to 10 August 2017, the airborne StratoClim mission took place in Kathmandu, Nepal where eight mission flights were conducted with the M-55 *Geophysica* up to altitudes of 20 km. New Particle Formation (NPF) was identified by the abundant presence of nucleation-mode aerosols, with particle diameters d_p smaller than 15 nm, which were *in-situ* detected by means of condensation nuclei (CN) counter techniques. NPF fields in clear-skies as well as in the presence of cloud ice particles (d_p > 3 µm) were encountered at upper troposphere / lowermost stratosphere (UT/LS) levels and within the Asian Monsoon Anticyclone (AMA). NPF-generated nucleation-mode particles in elevated concentrations (N_nm) were frequently found together with cloud ice (in number concentrations N_ice of up to 3 cm^{-3}) at heights between ~ 11 km and 16 km. From a total measurement time of ~ 22.5 hours above 10 km altitude, in-cloud NPF was in sum detected over ~ 1.3 hours (~ 50 % of all NPF records throughout StratoClim). Maximum N_nm of up to ~ 11000 cm^{-3} were detected coincidently with intermediate ice particle concentrations N_ice of 0.05 – 0.1 cm^{-3} at comparatively moderate carbon monoxide (CO) contents of ~ 90 - 100 nmol mol^{-1}. Neither under clear-sky nor during in-cloud NPF do the highest N_nm concentrations correlate with the highest CO mixing ratios, suggesting that an elevated pollutant load is not a prerequisite for NPF. Under clear-air conditions, NPF with elevated N_nm (> 8000 cm^{-3}) occurred slightly less often than within clouds. In the presence of cloud ice, NPF with N_nm between 1500 – 4000 cm^{-3} were observed about twice as often as under clear air conditions. NPF was not found when ice water contents exceeded 1000 µmol mol^{-1} in very cold air (< 195 K) at tropopause levels. This indicates a reduction of NPF once deep convection is prevalent together with the presence of mainly *liquid-origin* ice particles. Within *in-situ* cirrus near the cold point tropopause, recent NPF or intense events with mixing ration n_nm larger than 5000 mg^{-1} were observed only in about 6 % of the in-cloud NPF data. In determining whether the cloud-internal NPF is attenuated or prevented by the microphysical properties of cloud elements, the integral radius (*IR*) of the ice cloud population turned out to be indicative. Neither the number of ice particles nor the free distance between the ice particles are clearly related to the NPF-rate detected. While the increase of ice particles' mass per time ($\frac{\mathrm{d}m}{\mathrm{d}t}$) is proportional to the *IR* and mainly due to the condensation of water vapour, additional condensation of NPF precursor proceeds at the expense of the NPF rate as the precursor's saturation ratio declines. Numerical simulations show the impact of the *IR* on the supersaturation of a condensable vapour, such as sulphuric acid, and furthermore illustrate that the *IR* of the cloud ice determines the effective limitation of NPF-rates.

1. Introduction

The process of gas-to-particle conversion, also denoted as homogeneous aerosol nucleation and most commonly known as new particle formation (NPF), is a major source of atmospheric aerosols and cloud condensation nuclei, which could promote the cloud formation at intermediate and upper tropospheric altitudes (e.g. Spracklen et al. (2006); Merikanto et al. (2009); Dunne et al. (2016); Gordon et al. (2017)). Sulphuric acid (H_2SO_4) and water (H_2O) are important chemical compounds involved in the NPF process, which is aided when ions come into play at elevated altitudes and cold temperatures within the atmosphere (Lee et al. (2003); Kazil et al. (2008); Weigel et al. (2011); Duplissy et al. (2016)). It was suggested that a ternary nucleation process involves, apart from sulphuric acid and water, an additional constituent such as ammonia (NH_3; Ball et al. (1999); Benson et al. (2009); Höpfner et al. (2019)). Experimental studies at the CLOUD (Cosmics Leaving OUtdoor Droplets) chamber confirmed that NPF rates are substantially elevated within this ternary H_2SO_4-H_2O-NH_3 System (e.g. Kirkby et al. (2011); Kürten et al. (2016); Kürten (2019)). In addition to sulphuric acid and ammonia, organic species (e.g. Metzger et al. (2010); Kerminen et al. (2010)) or amines (Kürten et al., 2018) may also promote particle nucleation and growth. Considering the amounts of organic aerosols (Murphy et al., 2006) and ammonia species (Höpfner et al., 2019) that were frequently found in aerosol particles at UT/TTL heights in the AMA during StratoClim 2017, NPF is likely promoted by such species in the UT and TTL region.

The results of individual CLOUD experiments (Kürten et al. (2015); Kürten et al. (2016)) under a variety of controlled conditions and at different and elevated concentrations of the H_2SO_4 solution, always at supersaturated states, show how strongly the nucleation rates are associated with the precursor concentrations. The time series of a nucleation event within the CLOUD chamber (supplementary material of Kirkby et al. (2011)) shows that the nucleation rate remains elevated as long as the amount of precursors is kept at a constant level. Under real conditions in the atmosphere, however, the concentration of precursor material is spatially and temporally highly variable (e.g. Speidel et al. (2007), Ranjithkumar et al. (2021), or Höpfner et al.

(2019)). Besides the precursor gas abundance, temperature determines the degree of supersaturation, which implies that even high precursor concentrations can yield weak NPF rates. Additionally, also temperature fluctuations at any (low) precursor concentrations can increase the local supersaturation and induce intense NPF (cf. Weigel et al. (2021a)).

For ternary or multi-component NPF, the degree of supersaturation as a function of temperature remains indeterminable if the respective concentration of the different substances is unknown as so far is the case for most atmospheric observations. The chamber experiments allow for studying the nucleation rate as a function of the precursor concentration at different temperatures, i.e. at varying supersaturation ratios, which are specific, but mostly unknown, with respect to the system of nucleating substances (involving H_2SO_4, H_2O, and NH_3). The complexity increases with sulphuric acid nucleation systems involving besides NH_3 also nitric acid (HNO_3) (Wang et al., 2020) or oxidised organic vapours (Riccobono et al., 2014), all of which are reported as promoting NPF at supersaturations lower than required for pure H_2SO_4 solutions. The role of organic substances in connection with NPF is of particular importance in the tropical UT/LS as has been indicated by (Schulz et al., 2018) and (Andreae et al., 2018). The influence of third or more substances possibly involved in the NPF process is not conclusively detectable or quantifiable in the nucleation-mode particle population due to the current lack of instrumentation capable of directly analysing the chemical composition of such small particles.

By means of ground based as well as airborne *in-situ* measurements, NPF was frequently observed to occur at various conditions and atmospheric altitudes (Kerminen et al., 2018). Recently, Williamson et al. (2019) compiled a comprehensive data set of *in-situ* NPF observations at altitudes from 180 m above sea level to up to ∼ 12 km, thereby covering a latitude range from 80° North to 70° South alongside the Americas, and by probing air over both oceans, the Pacific and the Atlantic. In tropical regions, most of the *in-situ* NPF observations were made below the level of zero net radiative heating, i.e. at altitudes where subsidence or cloud formation is still well capable to efficiently remove or scavenge aerosol particles. Investigations at high altitudes (i.e. > 12 km) concerning the occurrence of NPF within clouds or in their immediate vicinity are sparse; most of such observations are limited to tropospheric altitudes (e.g. Clarke and Kapustin (2002)). The region above tropospheric clouds seems favourable for NPF to occur, and possible reasons for this are discussed by Wehner et al. (2015). They found that the majority of their near-cloud NPF observations correlated with increased ultraviolet irradiance, so they concluded cloud edges to be a favourable environment for the production of precursor gases for the formation of new particles (*ibid.*). These authors argued that nucleation and particle growth is promoted by turbulences at the cloud edges, which also Radke and Hobbs (1991) already observed coincidently with abundant particles at increased relative humidity.

Furthermore, NPF was found to be an important process inside the convective outflows (e.g. Twohy et al. (2002); Waddicor et al. (2012)). From measurements in the upper troposphere it is commonly assumed that the occurrence of NPF is directly connected to deep convective cloud systems (e.g. de Reus et al. (2001); Clarke and Kapustin (2002); Weigelt et al. (2009); Andreae et al. (2018)). The relationship between NPF and ice clouds is discussed in this study, whilst the immediate connection of NPF and deep convective events is addressed in Weigel et al. (2021a).

During *in-situ* measurements aboard the NASA high altitude research aircraft WB-57, Lee et al. (2004) observed nucleation events inside subtropical and tropical cirrus clouds between 7 and 16 km over Florida. The same authors summarise that they found recent occurrence of NPF in 72 % of their measurements within clouds. Despite the conceptual notion that the presence of cloud elements generally inhibits the formation of new particles, Kazil et al. (2007) demonstrated by means of model simulations that new sulphate aerosol can form within ice clouds such as cirrus. New particles are also produced in the anvil region and cirrus decks of Mesoscale Convective Systems (MCS) over West Africa (Frey et al., 2011). The particular role of mid-latitude MCS as a source of freshly formed aerosol within the upper troposphere was already suggested by Twohy et al. (2002), based on the detection of increased concentrations of particles with size diameter (d_{p}) greater than 25 nm, concurrently with elevated particle volatility. In the region of the Tropical Transition Layer (TTL) over South America, Australia and West Africa, the *in-situ* measurements by Weigel et al. (2011) revealed nucleation-mode particles in elevated number concentrations from recent NPF. Based on coincident detections of abundant nucleation-mode particles together with cloud elements (i.e. ice particles of diameters $2.7\ \mu\mathrm{m} < d_{\mathrm{p}} < 1.6\ \mathrm{mm}$) at ice number concentrations always below $\sim 2\ \mathrm{cm}^{-3}$ the authors concluded that the occurrence of NPF is mainly limited by the number of cloud particles. The underlying notation is that the surfaces of the cloud elements either scavenge the NPF-produced aerosol particles or remove the nucleating vapour molecules prior to the NPF process.

Regarding the occurrence of NPF in conjunction with the presence of upper tropospheric ice clouds several unspecified details remain:

1) What are the sets of chemical species acting as NPF precursor?
2) Does NPF require (or not) contributions by cosmic radiation, by ions (Lovejoy et al. (2004); Kazil et al. (2008); Weigel et al. (2011)), or by chemical agents or catalysts (e.g. Kürten (2019))?
3) Which are the advantageous thermodynamic conditions for NPF within a cloud?
4) What are the conditions under which NPF is suppressed by the presence of ice particles of certain size and/or number?

5) What are the relative contributions from clear-air or in-cloud NPF to the aerosol population in the UT/LS?
6) Furthermore, it is of interest how the nucleation-mode particles from in-cloud NPF are processed:
    a. are the nucleation-mode particles dispersed as contribution to the clear-air background aerosol as soon as the cloud elements evaporate, or
    b. are the nucleation-mode particles scavenged by present ice particles?

Comprehensive understanding of these relationships and their influences under real atmospheric conditions is necessary, particularly for modelling purposes. Such insights allow for narrowing down the cloud type and properties as well as the location in the cloud where NPF preferentially occurs in order to obtain estimates of the importance of NPF in the cloud. In the context of the Asian Monsoon Anticyclone (AMA) it is important to clarify the origin of observed aerosol enhancements in the embedded Asian Tropopause Aerosol Layer (ATAL, cf. Vernier et al. (2011); Vernier et al. (2018)). NPF is an important source of aerosol particles which are then available for further processing to form the ATAL (Höpfner et al. (2019); He et al. (2019); Mahnke et al. (2021)). Furthermore, the relative contribution of in-cloud versus clear-air NPF is of importance in this context.

The Asian Monsoon Anticyclone (AMA) is a meteorological structure, which determines the regional circulation in the UT/LS between June and September. The AMA is associated with extensive deep convection capable of transporting polluted air from the regional boundary layer (BL) to high altitudes (e.g. Randel and Park (2006); Park et al. (2007), Vogel et al. (2014); Vogel et al. (2019)). The vertical upward transport within the Asian monsoon circulation is an effective pathway for young air from the BL (Vogel et al., 2019) to UT/LS altitudes, accompanied by pollutants, further gaseous material (Pan et al., 2016), and water vapour (Ploeger et al., 2013). The constituents of the uplifted young air from BL altitudes also comprise precursor material from anthropogenic (Vernier et al. (2015); Yu et al. (2015); Höpfner et al. (2019); Mahnke et al. (2021)) and other sources to develop and maintain the observed ATAL.

This study reports on the frequent occurrence of NPF in the presence of cloud ice in the tropopause region over the Indian subcontinent during the Asian monsoon season of the year 2017. All measurement data shown herein were acquired during StratoClim (in July/August 2017) based at Kathmandu, Nepal, and conducted with the M-55 *Geophysica* that operates up to 20 km altitude. NPF was observed with almost equivalent extent in clear-air as well as in the midst of cloud ice particles. This investigation summarises the various conditions under which NPF was observed coincidently with cloud ice particles. The caveats limiting the magnitude of encountered NPF are examined, as are the possibly constraining mechanisms imposed by the cloud elements' microphysical properties. The frequency of NPF observations in coincidence with elevated ice particle densities as well as in clear air highlights the importance of the tropopause region within the AMA as an effective source region of aerosols.

2 The StratoClim field campaign, instruments and methods

During the Asian monsoon season, between 27 July and 10 August 2017, a total of eight scientific flights was conducted above parts of the Indian subcontinent, out of Kathmandu, Nepal (27° 42' 3'' N, 85° 21' 42'' E) throughout StratoClim 2017 (cf. Figure 1). Some of these flights also led out of the Nepalese airspace, to east India, Bangladesh and the farthest north of the Bay of Bengal. The occurrence of NPF was encountered (cf. Figure 1) during each flight, either in clear air or in the presence of cloud (ice) particles.

2.1 Number concentration of sub-micrometre sized particles

The 4-channel continuous flow condensation particle counter COPAS (COndensation PArticle counting System; Weigel et al. (2009)) was used for measuring aerosol particle number concentrations. Particle detection and data storage occurred at 1 Hz frequency. The COPAS channels were set to different 50 %-detection particle diameters d_{p50} (i.e. 6 nm, 10 nm, and 15 nm). By counting aerosols (with d_{p50} = 10 nm) downstream of a heated (~ 270°C) sample flow line, a fourth COPAS channel measured particle concentrations of non-volatile (nv) or refractory particles (e.g. soot, mineral dust, metallic aerosol material as well as, e.g., organic material mixtures not evaporating at 270 °C, etc.). The measured data revealed that potential artefacts on the aerosol measurements due to the presence of ice particles, as suggested by Williamson et al. (2019), are largely excludable for the StratoClim data set (cf. Appendix A). For further details on the operation of COPAS during StratoClim 2017, the companion paper (Weigel et al., 2021a) provides further insights, as does the article with the technical introduction and characterisation of the COPAS device, the aerosol inlet system, and the particle vaporiser (Weigel et al., 2009). COPAS is an established instrument for high altitude application and its data were used and discussed in various studies (e.g. in Curtius et al. (2005); Borrmann et al. (2010); Frey et al. (2011); Weigel et al. (2011); Weigel et al. (2014); Schumann et al. (2017); Höpfner et al. (2019)).

2.2 Terminology and notations

Measured particle number concentrations *N* are provided in units of particle number per cubic centimetre of sampled air (ambient conditions). To compare aerosol observations from different pressure altitudes and, e.g., for correlations with mixing ratios of trace gases, COPAS measurements are also given as mixing ratio *n* in units of particles per milligram of air (mg^{-1}) as calculated based on the 1 Hz-resolved data of ambient static pressure and temperature (cf.

Section 2.5). With N_6 (N_{15}) as the number concentration of submicrometre-sized particles with diameter greater than 6 nm (15 nm), the number concentration of nucleation-mode particles (denoted as N_{nm}) is calculated from the difference $N_6 - N_{15} = N_{6\text{-}15}$. This concentration of nucleation-mode particles indicates recent NPF if the designated NPF criterion (Equation 1) is met:

$$0.8 \cdot N_6 - 1.2 \cdot N_{15} > 0\,. \qquad (1)$$

This criterion was reassessed for the StratoClim 2017 data set and accounts for the COPAS detectors' signal-to-noise ratio and the counting statistics. Further details concerning the criterion and the corrections applied to COPAS data are provided in Weigel et al. (2021a).

If compliant with the NPF criterion, a series of data points is a designated NPF *event* if measured number concentrations (or mixing ratios) of nucleation-mode particles continuously remain greater than zero over at least five consecutive seconds. The term NPF *event duration* refers to the contiguous and uninterrupted measurement time (the sum of consecutive measurement seconds) for which the definition of in-cloud NPF applies. Due to the detector's signal-to-noise-ratio and counting statistics, the given quantity and durations of too short events (over 1-5 seconds) bear uncertainties in the resulting number concentrations of newly formed particles and the event duration. With the mean airspeed of the M-55 *Geophysica* (~ 154 ± 39 m s^{-1}), the event definition implies that within five seconds a horizontal distance of ~ 770 m (in flight direction) is covered. The total of 308 individual detections of elevated N_{nm} coincide with the presence of cloud elements, 104 of which fulfilled the event criterion. Note that the in-cloud NPF events discussed herein are partially embedded in larger NPF fields, which are identified by successive and uninterrupted detections of elevated N_{nm}. One or more in-cloud NPF events can be subsets of widespread NPF events as those discussed by Weigel et al. (2021a) where also further details are provided concerning the persistence of the freshly formed particles in the nucleation mode, and the presence of non-volatile particles under NPF conditions during StratoClim 2017.

The NPF-rate and, hence, the intensity of NPF varies with the degree of supersaturation of the NPF precursor (Kirkby et al. (2011), Kürten et al. (2016)). For the StratoClim 2017 data set the strength of a NPF event is classified as

(1) *intense* NPF (often used synonymously with *most recent* NPF) if detected aerosol densities of nucleation-mode particles exceed
    - mixing ratios of 10000 mg^{-1} or
    - number concentrations of 5000 cm^{-3},

(2) *intermediate* NPF when number densities of nucleation-mode particles range at
    - mixing ratios of 1000 $mg^{-1} < n_{\mathrm{nm}} < 10000\ mg^{-1}$ or
    - number concentrations of 500 $cm^{-3} < N_{\mathrm{nm}} < 5000\ cm^{-3}$, and

(3) *weak* NPF when

- mixing ratios n_{nm} remain below 1000 mg^{-1}, or
- number concentrations N_{nm} of less than 500 cm^{-3} are detected.

As the persistence of the particles in the nucleation mode is short (i.e. a few hours only due to coagulation, cf. Weigel et al. (2021a)), an intense NPF event could still be in process when observed, or it had expired recently, i.e. 1-2 hours prior to the detection. For NPF encounters with low or intermediate n_{nm} (or N_{nm}), the conclusions concerning the event's age remain ambiguous since they can result from an proceeding event with a low NPF rate or from an event that had expired several hours ago.

2.3 Cloud particle and water vapour detection

The NIXE-CAPS (New Ice eXpEriment: Cloud and Aerosol Particle Spectrometer, in the following denoted as NIXE) was deployed during StratoClim for measuring the number size distribution in the cloud particles' diameter size range of 3 – 930 µm with 1 Hz resolution (Luebke et al. (2016); Costa et al. (2017); Afchine et al. (2018). The NIXE-CAPS consist of two detectors: the NIXE-CAS-DPOL (Cloud and Aerosol Spectrometer with Detection of POLarization) and the NIXE-CIPg (Cloud Imaging Probe – grayscale). The compiled measurement data of both independent detectors delivers microphysical properties, in terms of size and number, of particles with diameters ranging from 0.61 µm to 937 µm. The methods of post flight data processing and corrections were described by Luebke et al. (2016).

In the StratoClim 2017 data set, cloud particle detections were recognised as such when particles of diameters > 3 µm were encountered in numbers greater than zero. The number concentration of ice particles is denoted as N_{ice} (i.e. $N_{3\text{-}937\mu\mathrm{m}}$, for the number concentration of ice particles with diameters of 3 µm < d_{p} < 937 µm). The data of ice water content (*IWC*) used herein were ascertained by using the relationship of cloud particles' mass (m_{p}) to diameter (d_{p}) (Krämer et al. (2016); Luebke et al. (2016); Afchine et al. (2018)).

The closed-path Lyman-α photo-fragment fluorescence hygrometer FISH (Fast In situ Stratospheric Hygrometer; cf. Zöger et al. (1999) and Meyer et al. (2015)) allows for 1 Hz - resolved measurements of the atmosphere's gaseous and solid phase water, denoted as total water or H_2O_{tot}. The FISH detection of H_2O_{tot} covers mixing ratios of 1 - 1000 µmol mol^{-1} over atmospheric pressures ranging from 50 hPa to 500 hPa with an accuracy and precision of 6 – 8 % and 0.3 µmol mol^{-1}. The ice water content (*IWC*) was calculated by subtracting the H_2O_{Gas} (measured by another Lyman-α detector, FLASH, the FLuorescent Airborne Stratospheric Hygrometer) from H_2O_{tot}. For further details concerning the data processing, see Afchine et al. (2018). Dependent on ambient temperatures, the smallest *IWC* detectable by the FISH instrument is approximately between $1 \cdot 10^{-3}$ µmol mol^{-1} and $20 \cdot 10^{-3}$ µmol mol^{-1}, which corresponds to approximately $1 – 20 \cdot 10^{-4}$ mg m^{-3} (Afchine et al., 2018).

To cover the wide range of *IWC* observed during the StratoClim mission (from thousandths to thousands of µmol mol^{-1}) the complementary data sets of NIXE-CAPS and FISH concerning *IWC* were merged (cf. Krämer et al. (2020)).

2.4 Carbon monoxide

In the troposphere, carbon monoxide (CO) is a component of atmospheric pollution (Park et al., 2009), the main sources of which are both natural and anthropogenic (including combustion, and the oxidation of hydrocarbons). Measured CO mixing ratios are often used as dynamic tracer for air parcel transport. Typical CO mixing ratios range from unpolluted 50 nmol mol^{-1} up to mixing ratios well exceeding 700 nmol mol^{-1} in close vicinity to emission sources (Clerbaux et al. (2008), Park et al. (2009)). Inside the AMA and up to 15 km altitude, CO mixing ratios remain comparatively high ($\gtrsim$ 100 nmol mol^{-1}), while between 15 km and 20 km altitude the CO mixing ratios decrease monotonically down to $\sim$ 40 nmol mol^{-1} (Park et al., 2009).

During the StratoClim mission, the mixing ratio of CO was measured by means of the Tunable Diode Laser (TDL) technique implied in the revised version of the Cryogenically Operated Laser Diode (COLD) spectrometer. Compared to the previous instrument version (4 s temporal resolution, Viciani et al. (2008)), COLD-2 integrates improvements (Viciani et al., 2018) regarding:

1) an increased measurement’s resolution by a factor of four,
2) an enhanced in-flight sensitivity of the COLD-2 spectrometer (ranging at $\sim$ 2 nmol mol^{-1} at integration times of 1 s) , and
3) an accuracy of 3 % is specified for the CO measurement with COLD-2.

In the data set of simultaneous measurements of COPAS and COLD-2, minimum and maximum CO mixing ratios of 14 nmol mol^{-1} and 153 nmol mol^{-1} are included.

2.5 Data of ambient temperature and static pressure

The atmospheric temperature and pressure data were taken from the Unit for Connection with the Scientific Equipment (UCSE, Sokolov and Lepuchov (1998)), a part of the navigational system of the M-55 *Geophysica*. UCSE data are provided as 1 Hz - resolved ambient pressure (with an accuracy of ±1 hPa) and temperature (±2 K accuracy).

The potential temperature θ is calculated with 1 Hz resolution in compliance with the definition by the World Meteorological Organization (WMO, 1966). Note that for the given vertical temperature gradients and over the θ -range covered during StratoClim 2017 (i.e. up to

$\sim$ 477 K), the WMO recommended calculation of θ differs only by up to $\sim$ 1 K from the values obtained by using the recently reappraised θ-calculation (Baumgartner et al., 2020).

3 Observations and results

During StratoClim 2017, eight mission flights were conducted with a total of 36.6 flight hours, whereas over a total of 6.42 hours ice clouds were encountered at air temperatures colder than 240 K. The cirrus cloud observations are described and discussed by Krämer et al. (2020). Most of the in-cloud measurements during StratoClim 2017 were performed at temperatures $\lesssim$ 205 K, corresponding to potential temperatures above $\sim$ 355 K and geometric altitudes higher than $\sim$ 12 km. The clouds observed during the Asian monsoon season include: 1) *in-situ* cirrus, which had formed in dynamically calm situations associated with very slow updraught as well as 2) *liquid-origin* cirrus, the formation of which is connected to deep (including overshooting) convection with elevated uplift velocities (see Section 5.2), including ice clouds (e.g. anvils) associated with convective outflow.

At temperatures colder than 205 K, N_{ice} and IWC often reached values above their respective median of 0.031 cm^{-3} (blue dashed line in Figure 2 c) and $\sim$ 0.2 – 2 µmol mol^{-1} (cf. Figure 6). The highest observed IWC values at these temperatures reach up to 1000 µmol mol^{-1} with a maximum N_{ice} as high as 30 cm^{-3}. Moreover, the ice crystal sizes (not shown here) exceed their corresponding median, hence, comparatively large ice crystals were found up to and around the cold point tropopause. Such large particles were detected during flights in strong convection.

3.1 The distribution of NPF and the presence of cloud ice particles over day time

During a total of $\sim$ 22.5 hours of COPAS measurement time at altitudes above $\sim$ 10 km ($\theta \gtrsim$ 350 K) a total duration of 2 hours and 38 minutes was spent under NPF conditions in the TTL region ($\sim$ 11-17.5 km, $\sim$ 355 – 400 K, cf. (Weigel et al., 2021a)). Throughout the StratoClim 2017 mission, elevated number densities of nucleation-mode particles were observed coincidently with cloud particles ($N_{\mathrm{ice}} > 0$ cm^{-3}) over a total of about 1 hour and 17 minutes (cf. Table 1). The encountered in-cloud NPF events at altitudes between approximately 11 km and 16.5 km ($\sim$ 355 – 385 K) had a mean event duration of 14.5 seconds (ranging from one second to a maximum of about 300 seconds, median duration: 2 seconds).

In Figure 2, all NPF detections throughout the StratoClim mission are compiled in a one-day time series. The range of this time series is limited to the schedules of the eight mission flights between 03:30 (UTC) and 12:30 (UTC) corresponding to local times of 09:15 LT to 18:15 LT. The encounter of NPF is considered as clear-air observation (black data points in Figure 2) when cloud (ice) particle number concentration N_{ice} remained at 0 cm^{-3}. Coincident observations of NPF and cloud (ice) particles ($N_{\mathrm{ice}} > 0$ cm^{-3}) are highlighted by red points in Figure 2 (Panels a and c). The number of in-cloud NPF encounters exceeding different thresholds of measured particle number concentration N_{nm} (500 cm^{-3}, 1000 cm^{-3}, and 5000 cm^{-3}, Panel b of Figure 2) shows for StratoClim 2017 that the intense events of in-cloud NPF occurred predominantly in the late morning, well before local noon. The incidences of in-cloud NPF accumulate in the later morning hours as well as in the local afternoon. Temporal dependencies on daytime were not observed for the occurrence, severity or frequency of NPF.

3.2 Vertical distribution of nucleation-mode particles in presence/absence of cloud ice particles

Figure 3 displays the vertical distribution of NPF-generated nucleation-mode aerosols in terms of the mixing ratio n_{nm} as a function of potential temperature. The panel a) of Figure 3 depicts the clear-air observations of elevated n_{nm} (black) together with those when coincidently ice particles were detected (red). The coincident observation of ice particles and nucleation-mode aerosols is vertically limited to a range of potential temperatures from 355 K to 385 K (cf. also Table 1). Thereby, in-cloud NPF of intermediate strength was encountered together with convective overshooting up to altitudes above the mean tropopause height (~ 380 K, averaged over the StratoClim 2017 period and area of operation). Further above (above 385 K and up to ~ 400 K) and at altitudes below 355 K, exclusively clear-air NPF was sampled. As already indicated by Figure 2, also the vertical profiles in Figure 3 suggest that the strength of NPF was largely independent from the presence of cloud elements. The intermediate panels (c and d) in Figure 3 show the StratoClim NPF data after their separation into clear-air and in-cloud conditions. Figure 3c shows that in-cloud NPF observations were made during each of the eight mission flights (cf. Figure 1). During the first four flights (from 27 July through 02 August) no in-cloud NPF was found above 365 K since deep convection occurred more sparsely in the first half of the StratoClim mission period than in the second half (Bucci et al., 2020) . During the second half of the mission flights (04 to 10 August), the frequency and the spatial extent of in-cloud NPF events were increased.

The comparison of CO mixing ratios and NPF occurrence in the tropical UT/LS over West Africa (Weigel et al., 2011) suggested a link between NPF-rate and ground-level sources of NPF precursors. These precursors (likely sulphur compounds, possibly also organics) are thought to be efficiently lifted into the TTL region by convection and not completely removed by scavenging. NPF should most frequently occur in air enriched with precursor material and which experienced vertical uplift. According to the panels e and f of Figure 3, neither of both, clear-air or in-cloud NPF, exhibit n_{nm} maxima coincidently with highest CO mixing ratios. This is not a typical characteristic of only in-cloud NPF as is discussed in more detail in Weigel et al. (2021a). During in-cloud NPF, the highest densities of nucleation-mode particles were observed at moderate CO mixing ratios of ~ 90 - 100 nmol mol^{-1}. In air masses with lowest CO content (~ 40 - 60 nmol mol^{-1}), NPF was observed only above the tropopause ($\theta > 380$ K) and in the absence of ice particles with n_{nm} ranging from 300 mg^{-1} to a maximum of 2000 mg^{-1}.

Most intense NPF, i.e. with highest densities of nucleation-mode aerosols, were found below the tropopause (~ 380 K). In the presence of ice particles (as in clear air), intermediate n_{nm} values were also encountered at CO mixing ratios below ~ 70 nmol mol^{-1} at potential temperatures of 370 - 380 K. Under clear-air conditions, NPF occurred even at much lower CO mixing ratios (mainly from measurements on 29 and 31 July), which is shown by the n_{nm} vertical profile at altitudes above 385 K (Figure 3f). According to Figure 3, in-cloud NPF was predominantly found in an altitude band between 355 K and 385 K (corresponding to ~ 9 – 16.5 km) with n_{nm} in the range of about 1000 to 50000 mg^{-1} (~ 500 – 11000 cm^{-3}). The n_{nm} values of NPF in ice clouds do generally not differ from those of NPF under clear-sky conditions.

3.3 Statistics of NPF events in the presence of ice particles

The frequency of NPF occurrence in coincidence with ice particles is illustrated in Figure 4. The upper panel (Figure 4a) exhibits the absolute frequency of occurrence of number concentrations N_{nm} observed during NPF events. The graphs compile all measurements (more than 4600 samples of 1 Hz - resolved data, cf. Table 1), which comply with the NPF criterion (black), for a comparison with clear-air NPF events (green) and those, which were coincidently detected with ice particles (red). At heights of in-cloud NPF observations (i.e. between 355 K and 385 K), the number concentrations of particles larger than the nucleation mode, i.e. N_{15} and N_{65}, ranged (by median) at ~ 200 cm^{-3} < N_{15} < 1000 cm^{-3} (COPAS) and ~ 60 cm^{-3} < N_{65} < 150 cm^{-3} (UHSAS-A, Mahnke et al. (2021)). Two features are apparent:

1) Number concentrations N_{nm} of more than ~ 8000 cm^{-3} seem to be observed more frequently (about 1.5 times more often) in clear-air conditions. As the number of in-cloud NPF observations with $N_{\mathrm{nm}} > 8000$ cm^{-3} is comparably low (≤ 10 encounters), the statistics is likely insufficient for drawing further conclusions from this. Whether the presence of cloud ice constrains the chance to detect very recent NPF (resulting in high N_{nm}), is discussed in Section 6.
2) For NPF in the presence of cloud ice, number concentrations N_{nm} between 1500 - 4000 cm^{-3} were observed about twice as often as under clear-air conditions (Figure 4a).

Highest N_{nm} values are found mainly in the absence of deposition surfaces, which ice particles would provide. It seems less understandable why NPF should generate a particular range of N_{nm} more frequently in the presence of cloud ice. Further discussion on this issue is provided in Section 6.

Until this point, the presence or absence of ice particles was distinguished by the criteria $N_{\text{ice}} = 0\ \text{cm}^{-3}$ or $N_{\text{ice}} > 0\ \text{cm}^{-3}$, respectively. Figure 4b depicts the occurrence frequency of N_{nm} with ice particles $N_{\text{ice}} > 0\ \text{cm}^{-3}$ normalised to the occurrence frequency of N_{nm} of all NPF events (black curve in Figure 4a). More than 75 % of observed NPF cases with $2000\ \text{cm}^{-3} < N_{\text{nm}} < 4000\ \text{cm}^{-3}$ (~ 200 samples) were detected while ice particles were present. In Figure 4c, the occurrence frequencies of N_{nm} are compiled for various levels of number densities N_{ice}, which were normalised to N_{nm} at $N_{\text{ice}} > 0\ \text{cm}^{-3}$ (red curve in Figure 4a). Thresholds of N_{ice} are set with stepwise increasing number concentrations (by one order of magnitude), to investigate whether the NPF is eventually constrained or influenced by the ice particle number density.

Although very faint, so called sub-visible cirrus clouds were found to comprise very small ice particle number concentrations of $10^{-5}\ \text{cm}^{-3}$ (corresponding to 0.1 per litre, cf. Kübbeler et al. (2011); Spreitzer et al. (2017)). Sub-visible cirrus with $N_{\text{ice}} < 10^{-3}\ \text{cm}^{-3}$ are assumed to have negligible influence on the NPF process, as is also to conclude from Figure 4c. Therefore, a first threshold level is set to $N_{\text{ice}} > 10^{-3}\ \text{cm}^{-3}$ (magenta curve), followed by the threshold level of $N_{\text{ice}} > 10^{-2}\ \text{cm}^{-3}$ (corresponding to 1 – 10 ice particles per litre, blue curve), which still represents a comparatively small amount of N_{ice} within sub-visible cirrus clouds (cf. Thomas et al. (2002); Peter et al. (2003); Davis et al. (2010); Frey et al. (2011)). The maximum observed N_{ice} reached up to $\sim 3\ \text{cm}^{-3}$. Concerning the frequency of observed N_{nm}, the difference between $N_{\text{ice}} > 0\ \text{cm}^{-3}$ and $N_{\text{ice}} > 10^{-3}\ \text{cm}^{-3}$ appears negligibly small. This leaves to conclude, that elevated N_{nm} were mostly observed coincidently with ice crystal number densities greater than $10^{-3}\ \text{cm}^{-3}$. With rising N_{ice} level (above $10^{-2}\ \text{cm}^{-3}$), the occurrence frequency of the highest N_{nm} ($> \sim 5000\ \text{cm}^{-3}$) decreased. When N_{ice} exceeds $10^{-1}\ \text{cm}^{-3}$, the occurrence of $N_{\text{nm}} > 4500\ \text{cm}^{-3}$ is significantly reduced and $N_{\text{nm}} > 8500\text{cm}^{-3}$ were absent. At the highest observed N_{ice} of $\sim 3\ \text{cm}^{-3}$, NPF with $N_{\text{nm}} > 250\ \text{cm}^{-3}$ were not detected anymore.

Hence, events with highest NPF-rates occurred preferentially at low ice particle concentrations or in clear air. At a certain N_{ice} level ($\sim 3\ \text{cm}^{-3}$), the process of NPF appears to be suppressed in general agreement with earlier findings (Weigel et al., 2011) indicating the limitation of NPF by $2\ \text{cm}^{-3}$ of cloud ice particles with diameter larger than 2 µm. Among other incidences, a singularly observed event was discussed (*ibid.*), during which NPF appeared to be suppressed by abundant cloud ice particles, while on leaving the cloud the NPF re-emerged at almost previously observed concentrations of nucleation mode particles. These findings suggest that NPF is entirely prevented in cases when N_{ice} exceeds $2 - 3\ \text{cm}^{-3}$.

4 In-cloud NPF related to *IWC* and cloud particle number densities

4.1 The relationship between cloud ice and aerosols

Based on *in-situ* measurements over northern Australia and over West Africa, de Reus et al. (2009) investigated the relationship between the number density of submicron aerosol particles and the abundance of cloud particles at UT/LS levels. The authors provided aerosol and ice particle number concentrations averaged over the duration of various cloud encounters to determine the proportion of submicrometre-sized particles that potentially convert into cloud ice. In the context of homogeneous ice nucleation, a specific relationship between the number concentration of aerosol and of ice particles cannot be expected (Kärcher and Lohmann, 2002), whereas such a relationship is inherent in the ice clouds' heterogeneous freezing process. From their analyses, de Reus et al. (2009) concluded that a similar range of ice-aerosol-ratios is observable in the convective outflow of both, ordinary tropical convection (Australia) as well as of large, mesoscale convective systems (MCSs, West Africa).

Figure 5 depicts the StratoClim 2017 data correspondingly to the data presentation by de Reus et al. (2009) from UT measurements in 2005 during SCOUT-O3, over Darwin, Australia. Reference lines are included, which indicate the number of encountered cloud particles per number of submicrometre-sized aerosol particles. The two panels in Figure 5 comprise the identical set of data points of ice cloud encounters during StratoClim 2017, each of which are averaged over at least 10 seconds and up to ~ 23 minutes.

Several occasions were identified by de Reus et al. (2009) when comparatively high ratios with up to a few hundreds of aerosol particles remained non-activated per single ice particle. The cloud ice – aerosol – ratios, which were found in the Asian monsoon's convective outflow region, agree with previous observations (de Reus et al., 2009), which were limited to the blue shaded area in Figure 5. Total aerosol numbers of significantly less than a few hundreds per single ice particle were not observed during StratoClim 2017, not either by de Reus et al. (2009). Up to N_{10} of 700 cm^{-3} almost all StratoClim data result from measurements at mean ambient temperatures colder than -75 °C (i.e. the temperatures, at which the observations by de Reus et al. (2009) were made). Frequent observations were made at aerosol concentrations below 1000 cm^{-3}. Compared to previous findings, the StratoClim data set comprises more observations at cloud ice – aerosol - ratios between 1 : 3 000 and 1 : 500 000, including frequent events of elevated N_{10} (> 10^{3} cm^{-3}). High N_{10} of more than 6000 cm^{-3}, were observed at *IWC* values mostly below 10 µmol mol^{-1} (i.e. log (*IWC*, µmol mol^{-1}) ≈ 1, Figure 5a). The majority of observations were made at mean *IWC* values below ~ 300 µmol mol^{-1} (i.e. log (*IWC*, µmol mol^{-1}) ≈ 2.5), which rules out that the measured N_{10} were impacted by shattering artefacts from ice particles (cf. Appendix A). The majority of NPF occurrences (mostly at ambient air temperatures between – 50 °C and – 80 °C) coincide with cloud ice – aerosol – ratios between 1 : 3 000 and 1 : 500 000 (cf. Figure 5b). The data points with in-cloud NPF concentrate between ratios of 1 : 30 000 and 1 : 500 000 because as a consequence of NPF, the aerosol proportion in the cloud ice – aerosol – ratio is strongly elevated. Concentrations N_{10} of more than 1000 cm^{-3} were not detected at ratios greater than 1 : 3 000. For N_{10} above 500 cm^{-3} and for cloud ice – aerosol - ratios smaller than 1 : 30 000, i.e. where elevated total aerosol concentrations mostly coincide with lower ice particles densities (~ 10^{-3} – 10^{-1} cm^{-3}), the observations occurred during NPF. Cloud ice – aerosol – ratios greater than 1 : 3 000 were reached mostly in the absence of NPF.

As pointed out by de Reus et al. (2009), there are caveats inherent with this kind of analyses. The strength or efficiency of the aerosol activation is not straightforward to deduce from provided ratios of total aerosol and cloud particle numbers. Many interdependencies exist that may impact the illustrated relationship, such as

1) the altering of the aerosol particles (coagulation, condensation) or of the cloud elements (sedimentation) or
2) the mixing of air masses with different aerosol and/or variable vapour saturation characteristics (entrainment).

The type of ice formation process (*liquid origin* or *in-situ*) and the convection dynamics additionally affect the relationship of cloud elements and interstitial aerosol. Assigning nucleation-mode particles of thousands per cm^3 (or more) to result from NPF is straightforward. In contrast, N_{nm} of a few 10 - 100 cm^{-3} are potentially filtered by the NPF criterion, and are probably not identified as NPF event if detected together with total aerosol concentrations (N_{10}) of comparable numbers. Apart from demonstrating the reproducibility of earlier findings (de Reus et al., 2009), the dataset was extended by new observations at different conditions (including NPF) obtained from StratoClim measurements.

4.2 NPF in the *IWC-T* parameter space

Analyses in earlier cirrus-related studies concerning the clouds' ice water content (*IWC*) as a function of ambient air temperature provide insight into the processes inherent with the cirrus formation (Krämer et al., 2016). As introduced by Luebke et al. (2016), Krämer et al. (2016), and Wernli et al. (2016), a distinction of cirrus clouds regarding their formation mechanism is obtainable within the *IWC-T* parameter space. The cirrus forms *in-situ* at elevated altitudes and instantaneously at sufficiently cold temperatures. The *liquid-origin* cirrus cloud forms on convective uplift from initially liquid droplets at lower altitudes (and less cold temperatures). More specifically Wernli et al. (2016) distinguishes:

- *liquid-origin* cirrus: initially well-sized liquid cloud droplets freeze at almost thermodynamic equilibrium in the ambient temperature range 235 K < T < 273 K under nearly saturated conditions with respect to liquid water (relative humidity RH_w of ~ 100 %), but at high supersaturation with respect to ice ($RH_i \gg 100$ %), while at freezing level, the water can coexist in each of its three phases.

- *in-situ* cirrus: under exclusion of pre-existing large liquid cloud droplets, ice crystals nucleate heterogeneously (due to deposition freezing) or freeze homogeneously from tiny super-cooled aqueous solution droplets (Koop et al., 2000), which are designated as "too small to be considered as cloud droplets" (Wernli et al., 2016).

In Figure 6 the *IWC* versus ambient air temperatures is displayed for all cloud encounters throughout StratoClim 2017 as a function (colour code) of
a) the mixing ratio of nucleation-mode particles (i.e. $n_{6\text{-}15} = n_{\mathrm{nm}}$; Figure 6a),
b) the total mixing ratio n_6 of particles with $d_{\mathrm{p}} > 6$ nm (Figure 6b) and
c) the CO mixing ratio (Figure 6c), respectively.

The upper panel of Figure 6 includes two data sets: (1) all data from StratoClim 2017 in 1 Hz -- resolution (grey data points) and (2) only the resulting n_{nm} complying with the NPF criterion (colour coded data points). At very low ambient air temperatures (~ 200 K and colder) and for comparatively high *IWC* values, the $n_{6\text{-}15}$ (grey) data were available but many failed the NPF criterion. The absolute values of the mixing ratio n_6 of submicrometre-sized particles were relatively high (Figure 6b). The detection of likewise excessive mixing ratios n_{15} (without illustration) resulted in $n_{6\text{-}15}$ that did not exceed the specified threshold of the NPF criterion (cf. Section 1.1). Nevertheless, most of the $n_{6\text{-}15}$ data points, which failed the NPF criterion (cf. the grey points in Figure 6a), coincide with the mixing ratios n_6 reaching up to several thousands of mg^{-1}. It is not deducible from COPAS measurements how the enriched particle densities (n_6 and n_{15}) distribute over the diameter spectrum of the submicrometre-sized aerosols. It therefore remains open whether the restrained $n_{6\text{-}15}$ are due to expired NPF with particles' rapid coagulation (with background aerosol and cloud ice) out of the nucleation-mode size range (Weigel et al., 2021a), or whether the particle enrichment (consistently in n_6 and n_{15}) is due to larger particles that were lifted with deep convection. The main findings from these juxtapositions can be summarised as follows:

● The absence of NPF with *IWC* exceeding 1000 µmol mol^{-1} at very cold air (Figure 6) suggests that NPF is constrained as soon as deep convection prevails, due to the presence of predominantly *liquid-origin* ice particles. *IWC* exceeding 1000 µmol mol^{-1} at air temperatures colder than 200 K indicates that deep convection had occurred. These high *IWC* originated from cloud ice that formed from liquid droplets at lower altitudes, as the amount of water vapour in the air at such cold temperatures is not sufficient to achieve comparable *IWC* values. Thus, the formation of encountered cirrus cannot be attributed to any other than the *liquid-origin* process.

This feature was observed during the flights on 27 July and on 10 August 2017, respectively. Within the same temperature range ($T < 200$ K), only a few NPF events with intermediate n_{nm} of more than ~ 4000 $\mathrm{mg^{-1}}$ (log (n_{nm}, $\mathrm{mg^{-1}}$) $\gtrsim 3.6$, yellow and reddish colours in Figure 6a) were encountered offside from strong convection.

- In the presence of *in-situ* formed cirrus particles at cold temperatures (185 – 200 K), i.e. in or around the cold point tropopause region, NPF events with $n_{\mathrm{nm}} > 5000$ (i.e. log (n_{nm}, $\mathrm{mg^{-1}}$) > 3.7, orange and reddish colours in Figure 6a) or recent NPF bursts were rarely observed. When the cloud ice has formed *in-situ* (CO < 80 nmol $\mathrm{mol^{-1}}$, yellow, greenish and blue colours in Figure 6c), mostly weak NPF with $n_{\mathrm{nm}} < 1500$ $\mathrm{mg^{-1}}$ (i.e. log (n_{nm}, $\mathrm{mg^{-1}}$) < 3.2, bluish colours of data points in Figure 6a) was observed. These data also indicate that NPF proceeds in air with low CO content.

- Suppression of NPF by cloud particles (due to the large total surface area from their number density and particle size) could explain why the number of nucleation-mode particles remained below the NPF criterion threshold at high *IWC* albeit total particle mixing ratios (n_6 and n_{15}) were significantly elevated. It is unlikely that the abundance of submicrometre-sized particles of up to 11000 $\mathrm{cm^{-3}}$ originates from interstitial (non-activated) aerosols carried in the cloud without contributions from NPF. The large particle quantities observed (10^3 - 10^4 $\mathrm{mg^{-1}}$) and the moderate CO content of the air sampled ($\lesssim 100$ nmol $\mathrm{mol^{-1}}$) indicate a source of these particles at high altitudes. About 4 hours after an NPF event has expired, the event may not be detectable anymore due to the short persistence of the particles in the nucleation-mode size range (Weigel et al., 2021a). Hence, if the *IWC* values remained high over several hours due to deep convection, and if NPF had happened more than four hours prior to the measurements, then the nucleation mode particles have certainly coagulated to sizes beyond 15 nm in diameter.

- Air's low pollutant load is indicated by comparatively moderate or low CO mixing ratios between 50 and about 100 nmol $\mathrm{mol^{-1}}$ at ambient air temperatures of < 200 K (Figure 6c). For comparison, the NPF observed during the West African monsoon were associated with CO levels between 60 and 90 nmol $\mathrm{mol^{-1}}$ (Weigel et al., 2011). Observation of intermediate NPF ($n_{\mathrm{nm}} < 1500$ $\mathrm{mg^{-1}}$, log (n_{nm}, $\mathrm{mg^{-1}}$) $\lesssim 3.3$) in the midst of *in-situ* formed cloud ice in air with low pollutant load (CO < 80 nmol $\mathrm{mol^{-1}}$) indicates that recent convective uplift of polluted air is not a prerequisite for NPF to occur. Advection of air from elsewhere or chemical and/or photochemical conversion cause the accumulation of NPF precursors at UT/LS levels. In air with the highest CO content (> 100 nmol $\mathrm{mol^{-1}}$), the *IWC*-*T*-values (for $T > 200$ K, i.e. at lower altitudes) remain in expected ranges and they scatter within the limits of most frequent observations (dashed black lines in Figure 6) as obtained from earlier analyses (Krämer et al., 2016). At the highest CO content (> 100 nmol $\mathrm{mol^{-1}}$), the n_{nm} values predominantly remained below 5000 $\mathrm{mg^{-1}}$.

5 The dependency of NPF on the proximity to ice particles

5.1 NPF as a function of mean free distance between ice elements

Surfaces, such as those of ice particles, constitute sinks for the gaseous precursor species such as the H_2SO_4-H_2O system (Bogdan et al. (2006); Bogdan et al. (2013)) and the abundance of condensation surface reduces or even prevents the NPF process.

The free distance between the ice particles is quantified based on the measurements of N_{ice} and of the ice particles' mean mass radius $\overline{r_{\text{ice}}}$, (consider $\overline{r_{\text{ice}}}^3 \sim \frac{IWC}{N_{ice}}$). The mean free volume in between the ice particles (the inter-crystal volume, ICV per cm^3 of air) is calculated with the number N_{ice}^* of ice particles (instead of the particles' number concentration) as:

$$\boldsymbol{ICV} = \frac{\boldsymbol{V - \frac{4}{3} \pi \cdot \bar{r}_{\text{ice}}^3 \cdot N_{\text{ice}}^*}}{\boldsymbol{N_{\text{ice}}^*}}, \tag{2}$$

which basically subtracts the total ice volume from the sampled air volume ($V = 1\ \text{cm}^3$) and the division by N_{ice}^* yields the ICV. Consequently, the ICV represents the mean particle-free volume assuming a homogeneous distribution of ice crystals within the air volume. With a maximum of measured ice particles ($N_{\text{ice}}^* = 3$) together with the maximum detected ice particle radius of 100 µm, the subtraction $V - \frac{4}{3} \cdot \pi \cdot \bar{r}_{\text{ice}}^3 \cdot N_{\text{ice}}^*$ corresponds by the order of magnitude to a subtraction of $10^{-11}\ \text{cm}^{-3}$ from $1\ \text{cm}^{-3}$. Hence, the volume of ice is insignificant compared to the volume of air, and the ICV may be considered as a function of N_{ice}^* only. The mean inter-crystalline distance (ICD, in cm) is then calculated by:

$$\boldsymbol{ICD} = \sqrt[3]{\frac{\boldsymbol{ICV}}{\left(\frac{4}{3} \cdot \boldsymbol{\pi}\right)}}\ , \tag{3}$$

and the ICV is assumed as a sphere around each individual ice particle. The radius of each sphere represents the mean ice-free distance in any direction from the individual ice particle. Conceptually, this approach corresponds to the definition of the cloud elements' distance provided by Baumgartner and Spichtinger (2018).

Figure 7a depicts the number concentration of nucleation-mode particles (N_{nm}) as a function of the calculated ICD. The continuous colour transition of the data points in x-direction together with unchanged colouring in y-direction demonstrates the independence of N_{nm} from the ICD and rather illustrates the correlation between the number of ice particles and their distance. The present ice particles compete for the limited amount of available water vapour such that elevated number concentrations of ice particles mainly result from the abundance of small ice particles. Hence, by means of the number of ice particles only, it is not possible to constrain the occurrence and/or strength of NPF as a wide scattering of N_{nm} concentrations was observed at any *ICD* between about 1 cm and 10 cm.

Figure 7b shows the ice particles' mean mass radius $\overline{r_{\mathrm{ice}}}$ as a function of the *ICD* and the number of nucleation-mode particles. By means of the mean mass radius $\overline{r_{\mathrm{ice}}}$, two different cases were distinguished:

a) For smallest ice particle sizes ($\sim 3 \mu\mathrm{m} < \overline{r_{\mathrm{ice}}} < \sim 20\ \mu\mathrm{m}$, $\log(\overline{r_{\mathrm{ice}}}, \mu\mathrm{m}) \lesssim 1.3$), a dependency of the *ICD* on the particle size was discernible. For instance, smallest ice particles (bluish $\overline{r_{\mathrm{ice}}}$) predominantly coincided with short *ICD* of about 1 cm at elevated N_{ice}. Towards larger *ICD*, ice particle sizes continuously increased up to $\overline{r_{\mathrm{ice}}} \approx 20\ \mu\mathrm{m}$, which reflects the competition of the ice crystals for the available water vapour. Within the same interval of ice particle sizes ($\overline{r_{\mathrm{ice}}} < \sim 20\ \mu\mathrm{m}$), the concentrations N_{nm} scattered over almost two orders of magnitude (from $\sim 100\ \mathrm{cm}^{-3}$ to $\sim 10\,000\ \mathrm{cm}^{-3}$) up to *ICD* of ~ 10 cm without any obvious systematic.

b) In the presence of larger ice particles, $\overline{r_{\mathrm{ice}}} > \sim 30\ \mu\mathrm{m}$ ($1.3 < \log(\overline{r_{\mathrm{ice}}}, \mu\mathrm{m}) \lesssim 1.4$, orange and reddish colours), the *ICD* ranged from ~ 1 cm to values above ~ 10 cm. Hence, not only $\overline{r_{\mathrm{ice}}}$ determined the resulting *ICD,* but N_{ice} increasingly contributed as well. The concentrations N_{nm} were not at the highest when *ICD* values reached their maximum at ~ 10 cm. For largest particles sizes ($\overline{r_{\mathrm{ice}}} > \sim 30\ \mu\mathrm{m}$), the values of N_{nm} accumulate at ~ 400 - $4000\ \mathrm{cm}^{-3}$ over the entire range of *ICDs*.

As long as the mean ice particle radius remained below a few dozen µm, NPF was encountered with almost any resulting N_{nm} concentration. As shown in Figure 4 and summarised in Section 4.4, a wide scatter of N_{nm} was observed to occur largely independent from coincidently detected number N_{ice} of ice particles. Hence, the in-cloud NPF observed during StratoClim 2017 was almost unaffected by the ice particle number, as long as the mean ice particle size remained small enough (i.e. with $\overline{r_{\mathrm{ice}}} < 20\ \mu\mathrm{m}$).

The *IWC* combines both microphysical parameters of the observed ice clouds, particle size and number concentration. If N_{nm} over *ICD* are analysed as a function of *IWC,* systematics become visible (Figure 7c). At lower *IWC* ($< 1\ \mu\mathrm{mol\ mol}^{-1}$, $\log(IWC, \mathrm{nmol\ mol}^{-1}) \lesssim 0$, bluish and green colours) the *ICD*s were at the largest and observed NPF was of the highest intensity (N_{nm} of several thousands per cm^{3}). Between $1\ \mu\mathrm{mol\ mol}^{-1}$ and $10\ \mu\mathrm{mol\ mol}^{-1}$ (yellow colours), the maximum of N_{nm} throughout observed NPF events was reduced. The maximum N_{nm} was further reduced when *IWC* increased to values beyond $10\ \mu\mathrm{mol\ mol}^{-1}$. This result demonstrates that the maximum N_{nm} reached throughout in-cloud NPF is determined (in addition to the precursor gas concentration) by the combination of both, the ice particles' number concentration N_{ice} and their mean mass radius $\overline{r_{\text{ice}}}$.

5.2 NPF as a function of cloud elements' integral radius *IR*

The combined effect of cloud ice particles' number density and size on the detectable N_{nm} during in-cloud NPF motivates to investigate N_{nm} values as a function of the integral radius $IR = \overline{r_{\text{ice}}} \cdot N_{\text{ice}}$ of the ice particle population. The parameter *IR* was described, e.g., by Manton (1979), or Politovich and Cooper (1988), and is frequently used to characterise clouds' microphysical properties (e.g. Korolev and Mazin (2003); or Krämer et al. (2009)). *IWC* and *IR* are expected to be strongly related (also visible by the systematic sorting of data in Figure 8a) as the diffusive growth rate of an ice particle ($\frac{\mathrm{d}m}{\mathrm{d}t}$) is proportional to *IR* (see e.g. Pruppacher and Klett (2012)). The *IR* is the direct control variable for the mass increase per time by condensation (mainly of water vapour) on the surface of a cloud ice particle and thus for the particle's growth rate. At supersaturated NPF conditions, the NPF precursors condense on the cloud ice particles and the change of the ice particle's mass ($\frac{\mathrm{d}m}{\mathrm{d}t}$) from the condensation of a gaseous precursor converts into a reduction of the gaseous precursor concentration.

For almost all *IR* below 1 µm cm^{-3}, the N_{nm} concentrations were unsystematically scattered over the entire interval between ~ 100 cm^{-3} and ~ 10 000 cm^{-3}. Towards the highest *IR* (> 1 µm cm^{-3}), the maximum of observed N_{nm} continuously decreased. This reflects a limiting influence by the cloud ice on the maximum strength of occurring NPF (indicated by the diagonal grey-shaded bars in Figure 8). An exceptional feature is exhibited in Figure 8a with a high signal of N_{nm} (~ 3000 – 4000 cm^{-3}) amongst elevated *IR* (between ~ 4 and 10 µm cm^{-3}). This cluster of data points resulted from the measurements of two individual mission flights, on 27 July (~ 3000 cm^{-3} < N_{nm} < ~ 3500 cm^{-3}) and on 06 August (~ 3500 cm^{-3} < N_{nm} < ~ 4000 cm^{-3}), respectively. During these measuring periods, ice particle densities (N_{ice}) and the mean ice particle sizes (i.e. the particles' mean mass radius $\overline{r_{\text{ice}}}$) did not rise above 0.1 - 0.3 cm^{-3} and 25 - 50 µm. Neither N_{nm} nor the ice microphysics exceeded the range of moderate values. The two independent exceptions in the observational data indicate a local/temporal state of imbalance that could have been caused by:

1) intermediate NPF, which was just proceeding when measured or which had been completed very recently (cf. Weigel et al. (2021a); in such a case, the observed N_{nm} should rapidly (< 1 h) decay to values of ~ 1000 cm^{-3} due to coagulation), or
2) ice particles, which sediment from high altitudes into an area of currently active NPF, or

3) cooling of air accompanied with nucleation of ice, while the cooling is due to the air parcel's vertical displacement, which results from deep convection or gravity wave activity (cf. (Weigel et al., 2021a)).

The limiting influence by the cloud ice on the maximum strength of NPF as indicated by the majority of observations is explainable by the reduction of NPF precursor material due to its condensation onto present ice particle surfaces. The question arises whether the distance between the ice particles allows efficient absorption and sustained reduction of NPF precursor molecules, or whether such an effect exists only in the immediate vicinity of an ice particle. The effectiveness of such a process strongly depends on the diffusivity of the NPF precursor molecules. If the molecules of the NPF precursor are absorbed before the thermodynamic conditions for NPF are reached, then these molecules are removed and missing in the formation of molecular clusters as initial step in the nucleation process. Numerical analyses concerning the reduction of the saturation ratio of H_2SO_4 due to the presence of ice particles, which are coated with H_2SO_4 (as typical for cirrus particles at 10-20 km altitude; cf. Bogdan et al. (2006); Bogdan et al. (2013)) are described in Appendix B (see also Figure B- 1). Although the binary H_2SO_4-H_2O nucleation process alone is assumed as insufficient to explain atmospheric NPF (Bianchi et al. (2016); Kirkby et al. (2011)), the numerical analysis qualitatively applies also to saturated condensable vapours containing compounds other than H_2SO_4 (cf. Riccobono et al. (2014)).

The numerical analysis yielded that the precursor's saturation ratio decreases rapidly with increasing *IR*. As long as the ice particles' size remains small (radii < 10 µm) their influence on the saturation ratio of the NPF precursor is comparatively weak. As demonstrated for H_2SO_4 (cf. Appendix B), rising *IR* (combining ice particle size and number) constrains the production of high N_{nm}, or inhibit NPF at all. Note, only completely uncoated ice particles of pure water (which are excluded to exist in the UT/LS; cf. Bogdan et al. (2006); Bogdan et al. (2013)) would be ineffective condensation surfaces for H_2SO_4 vapour.

According to Figure 8a, the N_{nm}-range of 500-3000 cm^{-3} is most frequently observed over the range of detected *IR* values. Regarding Figure 4, Section 4.4, Figure 8, and the simulation of Appendix B, the following conclusions seem likely:

1) The maximum N_{nm} resulting from in-cloud NPF is determined by *IR*. Abundant ice particles of sufficient size are capable of reducing the saturation ratio of NPF precursors within time scales ranging from half an hour to a few hours. Consequently, intermediate or weak NPF events with low N_{nm} production occur most frequently in the presence of cloud ice. The probability to instrumentally identify weak NPF events decreases with decreasing N_{nm}.

2) These NPF limitations by the *IR* result from the StratoClim 2017 dataset and may not necessarily be of general validity. Further investigations at other locations and under variable conditions and dedicated laboratory experiments are necessary to confirm these limitations marked as grey bars in Figure 8, which do not represent sharply quantifiable relationships.
3) Coagulation additionally affects N_{nm} on time scales of a few hours (cf. Weigel et al. (2021a)).

According to the results in Figure 8, *IR* values of about 24 µm cm^{-3} (corresponding to N_{ice} of about 0.7-0.8 cm^{-3} and $\overline{r_{\mathrm{ice}}}$ of about 32 µm) constituted the uppermost limit for in-cloud NPF observation during StratoClim 2017. Below the *IR* limits marked with grey bars, in-cloud NPF is encountered largely unaffected by the presence of ice particles. It is emphasised that the grey bars primarily mark a region in the $IR - n_{\mathrm{nm}}$ parameter space where the duration of an exceedance of marked levels decreases with increasing *IR* and/or n_{nm}. Hence, the detection of these points becomes less likely, or the probability increases to miss such events when the values cross the marked levels.

Figure 8b depicts N_{nm} as a function of *IR* with reference to the CO mixing ratio. Neither samples with highest N_{nm} nor samples with highest *IR* were directly ascribable to polluted air recently lifted from the surface. Intense NPF (with $N_{\mathrm{nm}} > 5000$ cm^{-3}) was observed at CO mixing ratios ranging between ~ 90 and 100 nmol mol^{-1}, which indicates the air's moderate pollutant load or its moderate age. In less polluted air (CO mixing ratios below~ 70 nmol mol^{-1}), the *IR* reaches the highest values (up to ~ 24 µm cm^{-3}) which were observed together with elevated *IWC* (up to ~750 µmol mol^{-1}, i.e. log (*IWC*, nmol mol^{-1}) ≈ 0.88). Within low-polluted air, cloud ice particles mostly form *in-situ*. It is conceivable, that the *in-situ* cloud ice formation and NPF happens simultaneously and induced by the same process: e.g. by updraughts due to subjacent convection (pileus effect) or by (local) cooling due to gravity waves (cf. Weigel et al. (2021a)). At CO mixing ratios below 70 nmol mol^{-1}, the observed N_{nm} range at a few hundreds per cm^3 but systematically below 1000 cm^{-3}.

Based on NPF encountered during StratoClim, the air masses with low pollutant loads therefore still contain sufficient amounts of precursor material to supply intermediate NPF (100 cm^{-3} < N_{nm} < 1000 cm^{-3}). This differs from earlier findings from ground-based measurements at high mountain sites (at about 5 km altitude) in the Himalaya region by Venzac et al. (2008) or at the Jungfraujoch station (~ 3.5 km altitude) in the Swiss Alps by Bianchi et al. (2016) who attributed their frequent NPF observations to the advection of polluted air which rises up from the valleys towards the research stations. Williamson et al. (2019) found frequent NPF during measurements over the Atlantic and the Pacific, i.e. in certain distance away from sources of industrial pollution. Like for StratoClim 2017, low levels of pollution here were sufficient to support NPF. .

6 Summary and Conclusions

Between 27 July and 10 August 2017 the airborne StratoClim mission took place in Kathmandu, Nepal, comprising eight mission flights (~ 22.5 hours of COPAS measurement time above 10 km, $\theta \gtrsim 350$ K) up to altitudes of 20 km ($\theta \approx 475$ K) with the Russian high-altitude research aircraft M-55 *Geophysica*. New Particle Formation in the presence of cloud ice particles was analysed, as it was encountered in the UT/LS region of the Asian Monsoon Anticyclone (AMA) over northern India, Nepal and Bangladesh. Over the StratoClim observation period, in-cloud NPF was a frequently occurring phenomenon within the AMA associated with predominantly large convective cloud systems over the Himalayan foothills. Elevated concentrations of nucleation-mode particles (N_{nm}) generated by NPF were observed in hitherto unreported frequency together with ice particles ($N_{\mathrm{ice}} > 0$ cm^{-3}) at altitudes between ~ 11 km and 16.5 km (~ 355 - 385 K) and mainly at ambient temperatures colder than ~ 230 K. During StratoClim 2017, a total number of 104 in-cloud NPF events was observed over a total duration of 1 hour and 17 minutes (~ 5 % of the total data set, ~ 49 % of all observed NPF cases). Maximum concentrations of nucleation-mode particles of up to ~ 11000 cm^{-3} (≈ 50000 mg^{-1}) were detected coincidently with ice particles in concentrations N_{ice} of 0.05 – 0.1 cm^{-3} (correspondent to 50 - 100 ice particles per litre) at heights of approximately 15.5 km (~ 370 K).

The observations indicate the N_{nm}-range of 500-3000 cm^{-3} as most frequently observed during in-cloud NPF. Weak events with low NPF-rate occur most frequently in the presence of cloud ice, whilst the probability to instrumentally identify such weak events decreases with N_{nm}. Coagulation additionally affects elevated N_{nm} in time scales of a few hours (cf. Weigel et al. (2021a)). Consequently, the supposedly preferred N_{nm}-range results from superimposed effects, and it is a matter of probability and timing (delay between NPF event and observation) that the N_{nm}-range of 500-3000 cm^{-3} is most frequently observed in the presence of cloud ice.

Analyses of the StratoClim data set concerning the relationship between interstitial aerosol and the abundance of cloud particles in the UT/LS are consistent with the findings from earlier measurements (de Reus et al., 2009), and extended these by new observations under different conditions. When ice particles are abundant ($N_{\mathrm{ice}} > 0.5$ cm^{-3}), total aerosol number concentrations (N_{10}) remain generally between ~ 200 cm^{-3} and 700 cm^{-3}. In agreement with earlier findings (de Reus et al., 2009), the ratio of ice particle number and the number of submicrometre-sized aerosols did not significantly rise above 300 submicrometre-sized aerosols per ice particle at low air temperatures (< 200 K). Intense NPF, generating nucleation-mode particles of several thousands per cm^3, substantially decrease the ratio of number concentrations of ice particles to aerosols. However, such intense NPF was not observed at ratios larger than 1:3000, which indicates that the presence of cloud ice imposes limitations to NPF.

In-cloud NPF appears limited in the presence of predominantly *liquid-origin* ice particles with increased ice water content resulting from deep convection up to cold point tropopause levels. This is confirmed by coincidently measured CO content of the air sample: air's pollutant load and/or its recent surface contact do not determine the strength of in-cloud NPF. Otherwise, the most intensive NPF events should be have been found more frequently in air masses with highest CO content. When the cloud ice has formed *in-situ,* at low CO mixing ratios, NPF was observed although with reduced strength. However, it is not yet conclusively clarified whether the direct convective supply of precursor material from pollution in the boundary layer is an essential prerequisite for the occurrence of NPF in the UT/LS, or whether NPF together with the ice cloud formation are initialised in processed and diluted air masses. The observations suggest that sufficient amounts of NPF precursor accumulate at UT/LS altitude, which is not necessarily connected to air's recent vertical uplift. It remains speculative, and it should be subject of suitable numerical analyses, to which extent the vertically lifted ice particles themselves contribute as carrier for soluble NPF precursor gases such as SO_2, H_2SO_4, or others, e.g., if dissolved in the cloud elements' liquid phase at lower heights and released again at TTL altitudes after the cloud ice has sublimated. Comparatively slow processes, as air mass transport from elsewhere or the chemical and/or photochemical conversion at elevated altitudes may suffice to supply the reservoir of NPF precursors at UT/LS altitudes. NPF of highest intensity, however, was observed at moderate CO mixing ratios. Intense NPF seems suppressed in strong convective updraughts (cf. Section 4.2), either because of the intense dynamics inherent with convection, or because the precursor's saturation ratio of recently uplifted air does not suffice for NPF.

At the moment of observation, the age of the nucleation-mode aerosols (the delay between the NPF burst and the instrumental detection) as well as the aerosol's processing history is unknown. While the aerosol's persistence in the nucleation mode is limited, it is conceivable that the abundance of aerosols influences the local formation of ice particles, or that ice particles are coated by nucleation-mode aerosol material due to coagulation. Above certain sizes, the cloud ice elements are increasingly subject to sedimentation. On sedimentation to warmer ambient temperatures, the ice particles sublimate. The remnants of sublimated cloud ice consists of materials attributed to the initially NPF-generated nucleation-mode aerosols. It remains speculative whether or not, in terms of physico-chemical characteristics, the released aerosol material is comparable with the primary NPF-generated aerosol. The sublimation of coated ice particles and the release of aerosol material at intermediate altitudes provides nuclei for cloud entrainment and/or for cloud formation. It remains unquantified whether NPF near the surface (cf. Venzac et al. (2008) or Bianchi et al. (2016)) or the NPF at UT/LS altitudes contribute at the most to the availability of cloud condensation nuclei (CCN), which are supposed to promote cloud formation (Andreae et al., 2018) at the cloud condensation levels. The specific source contributions to the abundance of available CCN are as variable as the chemical species that may be involved in the NPF process.

Ice particles in sufficient number and size are well capable to reduce the saturation ratio of a NPF precursor such as H_2SO_4. This implies two conclusions: 1) in-cloud NPF is limited by abundant ice particles and 2) not only the number of ice particles limits the NPF occurrence but also the ice particles' size. The strength of in-cloud NPF depends on the integral radius *IR* ($= \overline{r_{\mathrm{ice}}} \cdot N_{\mathrm{ice}}$), which constitutes the control value of the ice particle's growth ($\frac{\mathrm{d}m}{\mathrm{d}t}$). Up to *IR* of $\sim 1\ \mu\mathrm{m\ cm^{-3}}$ the occurrence of NPF of any strength (with $\sim 100 < N_{\mathrm{nm}} < 10\,000\ \mathrm{cm^{-3}}$) seems independent on the presence of ice particles at all. At larger *IR* ($> 1\ \mu\mathrm{m\ cm^{-3}}$) the presence of ice particles limits the maximum of N_{nm} from NPF. This result refines earlier conclusions (Weigel et al., 2011) according to which mainly the number of ice particles would limit the occurrence of NPF.

Data availability:

The data shown in this study are available at the StratoClim campaign database at

https://stratoclim.icg.kfa-juelich.de/AfcMain/CampaignDataBase ;

alternatively, they may be provided by respective PI upon request.

Author contribution

RW evaluated and analysed the data, created the figures, and drafted the manuscript with contributions by CM, MB, MK, HT and PS. SB participated in the data analyses and the manuscript drafting. Numerical simulations concerning the impact of ice particles on the saturation ratio of H_2SO_4 were performed by MB with contributions by HT. MK, NS, AA and CR contributed with cloud microphysical and water vapour data. SV and FD'A provided the CO data. The manuscript was critically reviewed by CM, MB, MK, PS, NS, AA, CR, SV, FD'A, HT, and SB.

Competing interests

The authors declare no competing interests.

Acknowledgements

The contributions from the workshops of the Max Planck Institute for Chemistry and of the Institute for Physics of the Atmosphere (Mainz University) were essential for this work. In particular, we acknowledge support of T. Böttger, M. Flanz, C. v. Glahn, H. Rott, and W. Schneider. Also acknowledged are the comprehensive and helpful discussions with M. Szakáll. We very much thank the crew of MDB (Myasishchev Design Bureau) and the M-55 *Geophysica* pilots. The extraordinary commitment of F. Stroh in realisation of the campaign and the leadership of the entire StratoClim project by M. Rex are gratefully acknowledged. Some of our research leading to the presented results received funding from the European Research Council under the European Union's Seventh Framework Program (FP/2007-2013)/ERC Grant Agreement No. 321040 (EXCATRO). The StratoClim project was funded by the EU (FP7/2007–2018 Grant No. 603557) and also supported by the German "Bundesministerium für Bildung und Forschung" (BMBF) under the joint ROMIC-project SPITFIRE (01LG1205A). M. Baumgartner acknowledges support by the DFG within the Transregional Collaborative Research CentreTRR165 "Waves to Weather", Project Z2. P. Spichtinger acknowledges support by the DFG within the research unit Multiscale Dynamics of Gravity Waves (MS-GWaves) through grant SP 1163/5-2. H. Tost acknowledges funding from the Carl-Zeiss foundation. We explicitly thank the officials of the Nepalese government authorities, research institutions and Tribhuvan Airport as well as of the German Embassy for their extraordinary support and hospitality, which enabled our field campaign and research.

Appendix A: Exclusion of sampling artefacts due to the presence of cloud ice

During the herein discussed NPF events, the detected total number concentration of cloud elements never exceeded ~2-3 cm^{-3}. Thus, the number density of cloud elements were always at least by two orders of magnitude smaller compared to detected aerosol number concentrations. At ambient air temperatures ranging from 187 K to 235 K, the clouds entirely consisted of ice particles. In other studies, however, the discussions on NPF are restricted to measurements under cloud-free (clear-air) conditions as the cloud particles are suspected to possibly impact onto the aircraft's hull or the aerosol inlet, this way possibly generating artefacts on the aerosol measurements (Williamson et al. (2019) referring to Weber et al. (1998)). Regarding the in-cloud NPF observations throughout StratoClim 2017, the following aspects are noteworthy:

1) At typical flight speeds of the M-55 *Geophysica* (154 ± 39 m s^{-1}), sub-micrometre-sized particles are not subject to impaction on parts of the aircraft structure (nose, wing's leading edge, etc.) as the particles follow the air stream around such flow obstacles (Kulkarni et al., 2011). Furthermore, ice particles in the diameter size range of a few micrometre (i.e. $1\ \mu m < d_p < 10\ \mu m$) partially sublimate in the congestion region upstream of any aircraft structure (e.g. the wings leading edge, or the aerosol inlet). The diffuser-type entry of the aerosol inlet leads to a flow deceleration inside the probe head accompanied with a sudden temperature increase (according to fluid dynamical simulations by up to 13°C on flow deceleration from 170 m s^{-1} to 60 m s^{-1}, cf. Weigel et al. (2009) and references therein). Hence, if a single particle with $1\ \mu m < d_p < 10\ \mu m$ randomly enters the COPAS aerosol inlet, rapid sublimation of such an ice particles can be expected to occur inside the aerosol inlet of COPAS. The entry of the sample air into

the inlet's second diffuser additionally reduces the sampling of ice particle fragments. Due to additional heating of the air sample and during their passage through the aerosol line to the COPAS detector (less than about 0.5 seconds), the ice particles from shattering with diameters of a few µm evaporate even if they are present in large numbers.

2) The number concentration of ice particles with diameter $d_p > 10$ µm mostly remained below 0.4 cm^{-3} when coincidently detected with NPF. On impact and shattering of a single ice particle of such a size, the number of generated fragments is estimated to range at about 10-100 per cm^3 (Korolev et al., 2013). Hence, to substantially affect the detected number concentration of nucleation-mode particles (on magnitude order of hundreds to up to ten thousands per cm^3), the number of ice particles emanating from shattering appears too low.
3) The probability that ice particles hit the sharp edged tips of the COPAS aerosol inlet (Weigel et al., 2009) appears negligibly small. The impaction surface provided by the COPAS aerosol inlet is mainly the inlet's ring-shaped entry with an opening diameter of ~ 7.3 mm and a wall thickness of ~ 100 µm. In the unlikely case that a single ice particle impact occurred, all generated fragments were required to endure the temperature rise within the inlet head (cf. first argument of this list) and the transport through the aerosol lines towards the COPAS detectors before they can cause any effect on the measurement.

An effect of shattered large ice particles on the detection of nucleation-mode particles is ultimately not excludable. However, despite the reference by Williamson et al. (2019) in this context, ice particle fragmentation was not described by Weber et al. (1998). The same authors discuss the influence on NPF detections due to fragmentation of super-cooled liquid-water cloud droplets and suggest a careful discussion in such cases. In general, such an influence due to the fragmentation of ice particles was largely ruled out or estimated as much lower than that of liquid droplets (Weber et al., 1998). Concerning the analyses discussed herein, however, it seems a statistical exception that ice particle fragments emanating from shattered ice particles crucially affect the measurement of the numbers of nucleation-mode particles. Moreover, if the NPF detections were systematically affected by the presence of cloud ice, the observed quantities of nucleation-mode particles would feature systematic and larger differences during in-cloud measurements compared to clear-air observations. None of the described artefacts was observable in the data from StratoClim 2017.

Appendix B: Impact of ice particles on NPF precursors' saturation ratio

Calculations were made regarding the time scales in which the decrease of the supersaturation of H_2SO_4 vapour occurs in the presence of coated ice particles. In the closest vicinity of an ice particle, the condensational loss of a precursor gas like sulphuric acid (H_2SO_4) predominates over the NPF process. The molecules' mobility and the condensation efficiency of the H_2SO_4 molecules is mainly determined by their diffusivity under the given atmospheric conditions. The diffusivity of H_2SO_4 is about a factor of 0.2-0.5 of the diffusivity of water vapour (Tang et al., 2014).

Presuming that the ice particles are coated with H_2SO_4 (Bogdan et al. (2006); Bogdan et al. (2013)), model simulations were performed to investigate the timescales in which the coated ice particles reduce various H_2SO_4 saturation ratios. The simulation results (shown in Figure B- 1) are based on constant ambient temperature ($T \approx 200$ K) and pressure ($p = 110$ hPa) conditions. For the same temperature conditions, the saturation vapour pressure p_{sat} of H_2SO_4 is calculated according to Vehkamäki et al. (2002). In this way, the degree of supersaturation is deducible from the H_2SO_4 molecules concentrations reported for the CLOUD (Cosmics Leaving OUtdoor Droplets) chamber experiments (cf. Kürten (2019), and references therein). According to this study, and in agreement with other references (H. Gordon, School of Earth and Environment, Leeds University, UK, personal communications Oct. 2019), molecule concentrations of $10^6 - 10^7$ cm^{-3} are required in the CLOUD chamber at temperatures of 208 K to induce NPF with nucleation rates of $10^{-2} - 100$ cm^{-3} s^{-1} (read out from Fig. 4 in Kürten (2019) from experiments at relative humidity of 38 %, *ibid.*). Keeping possible wall effects of the laboratory experiments in mind, for the occurrence of NPF under real atmospheric conditions, the lower bound of required molecule concentrations (10^6 cm^{-3}) may suffice, with an uncertainty of a factor five (H. Gordon, School of Earth and Environment, Leeds University, UK, personal communications Oct. 2019). At an ambient temperature of 208 K, the molecule concentrations of $10^6 - 10^7$ H_2SO_4 cm^{-3} (Kürten, 2019) correspond to saturation ratios of about $S \approx 10 - 100$. The following analysis, however, comprises a much wider range of saturation ratios between 10 and up to 5000 to account for a higher sensitivity of the temperature dependency of S.

Based on the expression formulated by Tsagkogeorgas et al. (2017) with the saturation vapour pressure p_{sat} of H_2SO_4 (above a flat surface) and with an accommodation coefficient of $\alpha = 0.65$ (Pöschl et al., 1998), the change of the fully coated ice crystal with mass m per time unit is calculated by:

$$\frac{\mathrm{d}m}{\mathrm{d}t} = \frac{4\pi D r(S-1)}{\left(\frac{L}{RT}-1\right)\frac{L}{T}\frac{D}{K}+\frac{RT}{\alpha \cdot p_{sat}}} \quad , \qquad (\mathrm{B}-1)$$

which conceptually represents the change of mass (size) of the particles, onto which the H_2SO_4 condenses and which is also consistent with the finding that cirrus cloud elements are coated with a H_2SO_4-H_2O layer (Bogdan et al. (2006); Bogdan et al. (2013)). The diffusivity of H_2SO_4 molecules in air is denoted with D, and K refers to the thermal conductivity of air, while R and R_{a} are the gas constants of H_2SO_4 and the air, respectively. Since the ice particles grow predominantly by the uptake of water vapour and the effective contribution to $\frac{\mathrm{d}m}{\mathrm{d}t}$ by the condensing H_2SO_4 is of minor concern. The $\frac{\mathrm{d}m}{\mathrm{d}t}$ from the condensing H_2SO_4 converts instead to a reduction in the saturation ratio of gaseous H_2SO_4, the change of which is:

$$\frac{\mathrm{d}S}{\mathrm{d}t} = -\frac{R}{R_a}\frac{p}{p_{sat}} N_{\mathrm{ice}} \frac{\mathrm{d}m}{\mathrm{d}t}\,, \quad (\mathrm{B}-2)$$

with the latent heat of vaporisation which is assumed as constant:

$$L = \frac{67.59 \cdot 10^3\ \mathrm{J\ mol^{-1}}}{M_{\mathrm{H2SO4}}}\,, \quad (\mathrm{B}-3)$$

and N_{ice} constitutes the number density of ice particles. Here, the sulphuric acid's molar mass is $M_{\mathrm{H2SO4}} = 0.098078\ \mathrm{kg\ mol^{-1}}$. Note, the combination of the equations B−2 and B−1 implies that $\frac{\mathrm{d}S}{\mathrm{d}t} \sim r \cdot N_{\mathrm{ice}}$, i.e. the temporal change of the precursor's saturation ratio is proportional to the integral radius *IR* considered in Section 5.2.

In Figure B- 1 the variability of two aspects is considered and in the panels (a-c) it is distinguished between three ice particle radii (1 µm, 10 µm, and 100 µm) and two different ice particle number concentrations (0.01 and 0.1 $\mathrm{cm^{-3}}$). The study by Ueyama et al. (2020) revealed that ice particles (effective radii of about 15 µm) persist over 12 to 20 hours at convective outflow levels between 365 K and 370 K potential temperature in the AMA of the 2017 season.

Based on the simulation, the largest particles (r_p = 100 µm) are capable to efficiently suppress NPF. Particles of this size and in highest concentrations of 0.1 $\mathrm{cm^{-3}}$ cause the saturation ratio to abate to saturation level (i.e. $S = 1$) within 20-50 minutes. At lower concentrations (0.01 $\mathrm{cm^{-3}}$) of particles of 100 µm radius, the saturation ratio is reduced by more than 70 % within 1 hour. Particles of 10 µm radius and in concentrations of 0.1 $\mathrm{cm^{-3}}$ are almost equally efficient in reducing the saturation ratio by ~ 70 % within 1 hour. Smaller number concentrations of the same particle size range, and smaller particles (r_p = 1 µm) require considerably more time than 1 hour to reduce the H_2SO_4 saturation ratio.

In essence, cloud ice particles can rapidly reduce the saturation ratio of H_2SO_4 as also of other condensable gases. The ranges of N_{ice} (0.01 - 0.1 $\mathrm{cm^{-3}}$) and particle size (1 µm < r_p < 100 µm) considered in the simulation correspond to the characteristics of ice particles coincidently observed with NPF throughout the StratoClim 2017 mission (note, away from NPF, higher N_{ice} and larger $\overline{r_{\mathrm{ice}}}$ were found, cf. Krämer et al. (2020)). About 71% of all ice cloud detections in coincidence with NPF had an *IR* (i.e. $\overline{r_{\mathrm{ice}}} \cdot N_{\mathrm{ice}}$) of less than 1 µm $\mathrm{cm^{-3}}$, while only about 1.5 % of the ice particle samples reached *IR* values greater than 7.5 µm $\mathrm{cm^{-3}}$; the maximum *IR* of 24 µm $\mathrm{cm^{-3}}$ was encountered once throughout the entire mission. In general, the cirrus cloud particles are expected as coated with a H_2SO_4/H_2O layer (Bogdan et al. (2006); Bogdan et al. (2013)) onto which sulphuric acid can condense. Impurities by weaker and substitutable acids (such as organic acids or HCl or HNO_3) also allow the H_2SO_4 uptake on the surface, which could reduce the gaseous H_2SO_4 concentration thereby suppressing NPF. Hence, in certain abundance the presence of cloud ice particles restrains the NPF process, when condensation prevails over the competing gas-to-particle conversion. The efficiency of condensation onto the ice particles' surface depends on

1) the size and number concentration of cloud ice particles and,
2) on the time interval during which the conditions remain at least saturated.

For the condensation of H_2SO_4, a partial coating of the ice particles' surface with sulphuric acid (or organic acids, HCl, or HNO_3) suffices to supply the gaseous H_2SO_4 with the required attachment points. To simplify the numerical simulation of the saturation decay, an ice particle is assumed as entirely coated (consistent with Bogdan et al. (2006); Bogdan et al. (2013)) and the (real) ice particle's habit (e.g. asphericity, porosity, etc.) remains unconsidered. Sporadic updraughts due to convective lifting well below the NPF level or gravity waves cause small-scaled expansion and cooling which increases the precursor's supersaturation (Weigel et al., 2021a). Certain concentrations of H_2SO_4 molecules exceed the supersaturation threshold for NPF, even in the presence of abundant cloud ice, as long as the NPF process occurs faster than the reduction of S due to the present ice.

References

Afchine, A., Rolf, C., Costa, A., Spelten, N., Riese, M., Buchholz, B., Ebert, V., Heller, R., Kaufmann, S., Minikin, A., Voigt, C., Zöger, M., Smith, J., Lawson, P., Lykov, A., Khaykin, S., and Krämer, M.: Ice particle sampling from aircraft - influence of the probing position on the ice water content, Atmos Meas Tech, 11, 4015-4031, 10.5194/amt-11-4015-2018, 2018.

Andreae, M. O., Afchine, A., Albrecht, R., Holanda, B. A., Artaxo, P., Barbosa, H. M. J., Borrmann, S., Cecchini, M. A., Costa, A., Dollner, M., Fütterer, D., Järvinen, E., Jurkat, T., Klimach, T., Konemann, T., Knote, C., Krämer, M., Krisna, T., Machado, L. A. T., Mertes, S., Minikin, A., Pöhlker, C., Pöhlker, M. L., Pöschl, U., Rosenfeld, D., Sauer, D., Schlager, H., Schnaiter, M., Schneider, J., Schulz, C., Spanu, A., Sperling, V. B., Voigt, C., Walser, A., Wang, J., Weinzierl, B., Wendisch, M., and Ziereis, H.: Aerosol characteristics and particle production in the upper troposphere over the Amazon Basin, Atmos Chem Phys, 18, 921-961, 10.5194/acp-18-921-2018, 2018.

Ball, S. M., Hanson, D. R., Eisele, F. L., and McMurry, P. H.: Laboratory studies of particle nucleation: Initial results for H_2SO_4, H_2O, and NH_3 vapors, J Geophys Res-Atmos, 104, 23709-23718, 10.1029/1999jd900411, 1999.

Baumgartner, M., and Spichtinger, P.: Towards a bulk approach to local interactions of hydrometeors, Atmos Chem Phys, 18, 2525-2546, 10.5194/acp-18-2525-2018, 2018.

Baumgartner, M., Weigel, R., Harvey, A. H., Ploeger, F., Achatz, U., and Spichtinger, P.: Reappraising the appropriate calculation of a common meteorological quantity: potential temperature, Atmos. Chem. Phys., 20, 15585-15616, 10.5194/acp-20-15585-2020, 2020.

Benson, D. R., Erupe, M. E., and Lee, S. H.: Laboratory-measured H_2SO_4-H_2O-NH_3 ternary homogeneous nucleation rates: Initial observations, Geophys Res Lett, 36, Artn L1581810.1029/2009gl038728, 2009.

Bianchi, F., Tröstl, J., Junninen, H., Frege, C., Henne, S., Hoyle, C. R., Molteni, U., Herrmann, E., Adamov, A., Bukowiecki, N., Chen, X., Duplissy, J., Gysel, M., Hutterli, M., Kangasluoma, J., Kontkanen, J., Kürten, A., Manninen, H. E., Münch, S., Peräkylä, O., Petäjä, T., Rondo, L., Williamson, C., Weingartner, E., Curtius, J., Worsnop, D. R., Kulmala, M., Dommen, J., and Baltensperger, U.: New particle formation in the free troposphere: A question of chemistry and timing, Science, 352, 1109-1112, 10.1126/science.aad5456, 2016.

Bogdan, A., Molina, M. J., Sassen, K., and Kulmala, M.: Formation of low-temperature cirrus from H_2SO_4/H_2O aerosol droplets, J Phys Chem A, 110, 12541-12542, 10.1021/jp065898e, 2006.

Bogdan, A., Molina, M. J., Kulmala, M., Tenhu, H., and Loerting, T.: Solution coating around ice particles of incipient cirrus clouds, P Natl Acad Sci USA, 110, E2439-E2439, 10.1073/pnas.1304471110, 2013.

Borrmann, S., Kunkel, D., Weigel, R., Minikin, A., Deshler, T., Wilson, J. C., Curtius, J., Volk, C. M., Homan, C. D., Ulanovsky, A., Ravegnani, F., Viciani, S., Shur, G. N., Belyaev, G. V., Law, K. S., and Cairo, F.: Aerosols in the tropical and subtropical UT/LS: in-situ measurements of submicron particle abundance and volatility, Atmos Chem Phys, 10, 5573-5592, 10.5194/acp-10-5573-2010, 2010.

Bucci, S., Legras, B., Sellitto, P., D'Amato, F., Viciani, S., Montori, A., Chiarugi, A., Ravegnani, F., Ulanovsky, A., Cairo, F., and Stroh, F.: Deep-convective influence on the upper troposphere–lower stratosphere composition in the Asian monsoon anticyclone region: 2017 StratoClim campaign results, Atmos. Chem. Phys., 20, 12193-12210, 10.5194/acp-20-12193-2020, 2020.

Clarke, A. D., and Kapustin, V. N.: A pacific aerosol survey. Part I: A decade of data on particle production, transport, evolution, and mixing in the troposphere, Journal of the Atmospheric Sciences, 59, 363-382, 10.1175/1520-0469(2002)059<0363:Apaspi>2.0.Co;2, 2002.

Clerbaux, C., George, M., Turquety, S., Walker, K. A., Barret, B., Bernath, P., Boone, C., Borsdorff, T., Cammas, J. P., Catoire, V., Coffey, M., Coheur, P. F., Deeter, M., De Maziere, M., Drummond, J., Duchatelet, P., Dupuy, E., de Zafra, R., Eddounia, F., Edwards, D. P., Emmons, L., Funke, B., Gille, J., Griffith, D. W. T., Hannigan, J., Hase, F., Hopfner, M., Jones, N., Kagawa, A., Kasai, Y., Kramer, I., Le Flochmoen, E., Livesey, N. J., Lopez-Puertas, M., Luo, M., Mahieu, E., Murtagh, D., Nedelec, P., Pazmino, A., Pumphrey, H., Ricaud, P., Rinsland, C. P., Robert, C., Schneider, M., Senten, C., Stiller, G., Strandberg, A., Strong, K., Sussmann, R., Thouret, V., Urban, J., and Wiacek, A.: CO measurements from the ACE-FTS satellite instrument: data analysis and validation using ground-based, airborne and spaceborne observations, Atmos Chem Phys, 8, 2569-2594, 10.5194/acp-8-2569-2008, 2008.

Costa, A., Meyer, J., Afchine, A., Luebke, A., Gunther, G., Dorsey, J. R., Gallagher, M. W., Ehrlich, A., Wendisch, M., Baumgardner, D., Wex, H., and Kramer, M.: Classification of Arctic, midlatitude and tropical clouds in the mixed-phase temperature regime, Atmos Chem Phys, 17, 12219-12238, 10.5194/acp-17-12219-2017, 2017.

Curtius, J., Weigel, R., Vössing, H. J., Wernli, H., Werner, A., Volk, C. M., Konopka, P., Krebsbach, M., Schiller, C., Roiger, A., Schlager, H., Dreiling, V., and Borrmann, S.: Observations of meteoric material and implications for aerosol nucleation in the winter Arctic lower stratosphere derived from in situ particle measurements, Atmos Chem Phys, 5, 3053-3069, 10.5194/acp-5-3053-2005, 2005.

Davis, S., Hlavka, D. L., Jensen, E. J., Rosenlof, K., Yang, Q., Schmidt, S., Borrmann, S., Frey, W., Lawson, P., Voemel, H., and Bui, T. P.: In situ and lidar observations of tropopause subvisible cirrus clouds during TC4, Journal of Geophysical Research: Atmospheres, 115, 10.1029/2009jd013093, 2010.

de Reus, M., Krejci, R., Williams, J., Fischer, H., Scheele, R., and Strom, J.: Vertical and horizontal distributions of the aerosol number concentration and size distribution over the northern Indian Ocean, J Geophys Res-Atmos, 106, 28629-28641, Doi 10.1029/2001jd900017, 2001.

de Reus, M., Borrmann, S., Bansemer, A., Heymsfield, A. J., Weigel, R., Schiller, C., Mitev, V., Frey, W., Kunkel, D., Kurten, A., Curtius, J., Sitnikov, N. M., Ulanovsky, A., and Ravegnani, F.: Evidence for ice particles in the tropical stratosphere from in-situ measurements, Atmos Chem Phys, 9, 6775-6792, DOI 10.5194/acp-9-6775-2009, 2009.

Dunne, E. M., Gordon, H., Kürten, A., Almeida, J., Duplissy, J., Williamson, C., Ortega, I. K., Pringle, K. J., Adamov, A., Baltensperger, U., Barmet, P., Benduhn, F., Bianchi, F., Breitenlechner, M., Clarke, A., Curtius, J., Dommen, J., Donahue, N. M., Ehrhart, S., Flagan, R. C., Franchin, A., Guida, R., Hakala, J., Hansel, A., Heinritzi, M., Jokinen, T., Kangasluoma, J., Kirkby, J., Kulmala, M., Kupc, A., Lawler, M. J., Lehtipalo, K., Makhmutov, V., Mann, G., Mathot, S., Merikanto, J., Miettinen, P., Nenes, A., Onnela, A., Rap, A., Reddington, C. L. S., Riccobono, F., Richards, N. A. D., Rissanen, M. P., Rondo, L., Sarnela, N., Schobesberger, S., Sengupta, K., Simon, M., Sipilä, M., Smith, J. N., Stozkhov, Y., Tomé, A., Tröstl, J., Wagner, P. E., Wimmer, D., Winkler, P. M., Worsnop, D. R., and Carslaw, K. S.: Global atmospheric particle formation from CERN CLOUD measurements, Science, 354, 1119-1124, 10.1126/science.aaf2649, 2016.

Duplissy, J., Merikanto, J., Franchin, A., Tsagkogeorgas, G., Kangasluoma, J., Wimmer, D., Vuollekoski, H., Schobesberger, S., Lehtipalo, K., Flagan, R. C., Brus, D., Donahue, N. M., Vehkamaki, H., Almeida, J., Amorim, A., Barmet, P., Bianchi, F., Breitenlechner, M., Dunne, E. M., Guida, R., Henschel, H., Junninen, H., Kirkby, J., Kurten, A., Kupc, A., Maattanen, A., Makhmutov, V., Mathot, S., Nieminen, T., Onnela, A., Praplan, A. P., Riccobono, F., Rondo, L., Steiner, G., Tome, A., Walther, H., Baltensperger, U., Carslaw, K. S., Dommen, J., Hansel, A., Petaja, T., Sipila, M., Stratmann, F., Vrtala, A., Wagner, P. E., Worsnop, D. R., Curtius, J., and Kulmala, M.: Effect of ions on sulfuric acid-water binary particle formation: 2. Experimental data and comparison with QC-normalized classical nucleation theory, J Geophys Res-Atmos, 121, 1752-1775, 10.1002/2015jd023539, 2016.

Frey, W., Borrmann, S., Kunkel, D., Weigel, R., de Reus, M., Schlager, H., Roiger, A., Voigt, C., Hoor, P., Curtius, J., Kramer, M., Schiller, C., Volk, C. M., Homan, C. D., Fierli, F., Di Donfrancesco, G., Ulanovsky, A., Ravegnani, F., Sitnikov, N. M., Viciani, S., D'Amato, F., Shur, G. N., Belyaev, G. V., Law, K. S., and Cairo, F.: In situ measurements of tropical cloud properties in the West African Monsoon: upper tropospheric ice clouds, Mesoscale Convective System outflow, and subvisual cirrus, Atmos Chem Phys, 11, 5569-5590, DOI 10.5194/acp-11-5569-2011, 2011.

Gordon, H., Kirkby, J., Baltensperger, U., Bianchi, F., Breitenlechner, M., Curtius, J., Dias, A., Dommen, J., Donahue, N. M., Dunne, E. M., Duplissy, J., Ehrhart, S., Flagan, R. C., Frege, C., Fuchs, C., Hansel, A., Hoyle, C. R., Kulmala, M., Kürten, A., Lehtipalo, K., Makhmutov, V., Molteni, U., Rissanen, M. P., Stozkhov, Y., Tröstl, J., Tsagkogeorgas, G., Wagner, R., Williamson, C., Wimmer, D., Winkler, P. M., Yan, C., and Carslaw, K. S.: Causes and importance of new particle formation in the present-day and preindustrial atmospheres, Journal of Geophysical Research: Atmospheres, 122, 8739-8760, 10.1002/2017jd026844, 2017.

He, Q., Ma, J., Zheng, X., Yan, X., Vömel, H., Wienhold, F. G., Gao, W., Liu, D., Shi, G., and Cheng, T.: Observational evidence of particle hygroscopic growth in the upper troposphere–lower stratosphere (UTLS) over the Tibetan Plateau, Atmos. Chem. Phys., 19, 8399-8406, 10.5194/acp-19-8399-2019, 2019.

Höpfner, M., Ungermann, J., Borrmann, S., Wagner, R., Spang, R., Riese, M., Stiller, G., Appel, O., Batenburg, A. M., Bucci, S., Cairo, F., Dragoneas, A., Friedl-Vallon, F., Hünig, A., Johansson, S., Krasauskas, L., Legras, B., Leisner, T., Mahnke, C., Möhler, O., Molleker, S., Müller, R., Neubert, T., Orphal, J., Preusse, P., Rex, M., Saathoff, H., Stroh, F., Weigel, R., and Wohltmann, I.: Ammonium nitrate particles formed in upper troposphere from ground ammonia sources during Asian monsoons, Nat Geosci, 12, 608-612, 10.1038/s41561-019-0385-8, 2019.

Kärcher, B., and Lohmann, U.: A parameterization of cirrus cloud formation: Homogeneous freezing of supercooled aerosols, J Geophys Res-Atmos, 107, 4010, 10.1029/2001jd000470, 2002.

Kazil, J., Lovejoy, E. R., Jensen, E. J., and Hanson, D. R.: Is aerosol formation in cirrus clouds possible?, Atmos Chem Phys, 7, 1407-1413, DOI 10.5194/acp-7-1407-2007, 2007.

Kazil, J., Harrison, R. G., and Lovejoy, E. R.: Tropospheric new particle formation and the role of ions, Space Sci Rev, 137, 241-255, 10.1007/s11214-008-9388-2, 2008.

Kerminen, V. M., Petaja, T., Manninen, H. E., Paasonen, P., Nieminen, T., Sipila, M., Junninen, H., Ehn, M., Gagne, S., Laakso, L., Riipinen, I., Vehkamaki, H., Kurten, T., Ortega, I. K., Dal Maso, M., Brus, D., Hyvarinen, A., Lihavainen, H., Leppa, J., Lehtinen, K. E. J., Mirme, A., Mirme, S., Horrak, U., Berndt, T., Stratmann, F., Birmili, W., Wiedensohler, A., Metzger, A., Dommen, J., Baltensperger, U., Kiendler-Scharr, A., Mentel, T. F., Wildt, J., Winkler, P. M., Wagner, P. E., Petzold, A., Minikin, A., Plass-Dulmer, C., Poschl, U., Laaksonen, A., and Kulmala, M.: Atmospheric nucleation: highlights of the EUCAARI project and future directions, Atmos Chem Phys, 10, 10829-10848, 10.5194/acp-10-10829-2010, 2010.

Kerminen, V. M., Chen, X. M., Vakkari, V., Petäjä, T., Kulmala, M., and Bianchi, F.: Atmospheric new particle formation and growth: review of field observations, Environ Res Lett, 13, Artn 10300310.1088/1748-9326/Aadf3c, 2018.

Kirkby, J., Curtius, J., Almeida, J., Dunne, E., Duplissy, J., Ehrhart, S., Franchin, A., Gagne, S., Ickes, L., Kurten, A., Kupc, A., Metzger, A., Riccobono, F., Rondo, L., Schobesberger, S., Tsagkogeorgas, G., Wimmer, D., Amorim, A., Bianchi, F., Breitenlechner, M., David, A., Dommen, J., Downard, A., Ehn, M., Flagan, R. C., Haider, S., Hansel, A., Hauser, D., Jud, W., Junninen, H., Kreissl, F., Kvashin, A., Laaksonen, A., Lehtipalo, K., Lima, J., Lovejoy, E. R., Makhmutov, V., Mathot, S., Mikkila, J., Minginette, P., Mogo, S., Nieminen, T., Onnela, A., Pereira, P., Petaja, T., Schnitzhofer, R., Seinfeld, J. H., Sipila, M., Stozhkov, Y., Stratmann, F., Tome, A., Vanhanen, J., Viisanen, Y., Vrtala, A., Wagner, P. E., Walther, H., Weingartner, E., Wex, H., Winkler, P. M., Carslaw, K. S., Worsnop, D. R., Baltensperger, U., and Kulmala, M.: Role of sulphuric acid, ammonia and galactic cosmic rays in atmospheric aerosol nucleation, Nature, 476, 429-U477, 10.1038/nature10343, 2011.

Koop, T., Luo, B. P., Tsias, A., and Peter, T.: Water activity as the determinant for homogeneous ice nucleation in aqueous solutions, Nature, 406, 611-614, Doi 10.1038/35020537, 2000.

Korolev, A., Emery, E., and Creelman, K.: Modification and tests of particle probe tips to mitigate effects of ice shattering, Journal of Atmospheric and Oceanic Technology, 30, 690-708, 10.1175/JTECH-D-12-00142.1, 2013.

Korolev, A. V., and Mazin, I. P.: Supersaturation of Water Vapor in Clouds, Journal of the Atmospheric Sciences, 60, 2957-2974, 10.1175/1520-0469(2003)060<2957:sowvic>2.0.co;2, 2003.

Krämer, M., Schiller, C., Afchine, A., Bauer, R., Gensch, I., Mangold, A., Schlicht, S., Spelten, N., Sitnikov, N., Borrmann, S., de Reus, M., and Spichtinger, P.: Ice supersaturations and cirrus cloud crystal numbers, Atmos Chem Phys, 9, 3505-3522, 2009.

Krämer, M., Rolf, C., Luebke, A., Afchine, A., Spelten, N., Costa, A., Meyer, J., Zöger, M., Smith, J., Herman, R. L., Buchholz, B., Ebert, V., Baumgardner, D., Borrmann, S., Klingebiel, M., and Avallone, L.: A microphysics guide to cirrus clouds - Part 1: Cirrus types, Atmospheric Chemistry and Physics, 16, 3463-3483, 10.5194/acp-16-3463-2016, 2016.

Krämer, M., Rolf, C., Spelten, N., Afchine, A., Fahey, D., Jensen, E., Khaykin, S., Kuhn, T., Lawson, P., Lykov, A., Pan, L. L., Riese, M., Rollins, A., Stroh, F., Thornberry, T., Wolf, V., Woods, S., Spichtinger, P., Quaas, J., and Sourdeval, O.: A microphysics guide to cirrus – Part 2: Climatologies of clouds and humidity from observations, Atmos. Chem. Phys., 20, 12569-12608, 10.5194/acp-20-12569-2020, 2020.

Kübbeler, M., Hildebrandt, M., Meyer, J., Schiller, C., Hamburger, T., Jurkat, T., Minikin, A., Petzold, A., Rautenhaus, M., Schlager, H., Schumann, U., Voigt, C., Spichtinger, P., Gayet, J. F., Gourbeyre, C., and Krämer, M.: Thin and subvisible cirrus and contrails in a subsaturated environment, Atmos Chem Phys, 11, 5853-5865, 10.5194/acp-11-5853-2011, 2011.

Kulkarni, P., Baron, P. A., and Willeke, K.: Aerosol measurement: principles, techniques, and applications, John Wiley & Sons, 2011.

Kürten, A., Williamson, C., Almeida, J., Kirkby, J., and Curtius, J.: On the derivation of particle nucleation rates from experimental formation rates, Atmos Chem Phys, 15, 4063-4075, 10.5194/acp-15-4063-2015, 2015.

Kürten, A., Bianchi, F., Almeida, J., Kupiainen-Maatta, O., Dunne, E. M., Duplissy, J., Williamson, C., Barmet, P., Breitenlechner, M., Dommen, J., Donahue, N. M., Flagan, R. C., Franchin, A., Gordon, H., Hakala, J., Hansel, A., Heinritzi, M., Ickes, L., Jokinen, T., Kangasluoma, J., Kim, J., Kirkby, J., Kupc, A., Lehtipalo, K., Leiminger, M., Makhmutov, V., Onnela, A., Ortega, I. K., Petaja, T., Praplan, A. P., Riccobono, F., Rissanen, M. P., Rondo, L., Schnitzhofer, R., Schobesberger, S., Smith, J. N., Steiner, G., Stozhkov, Y., Tome, A., Trostl, J., Tsagkogeorgas, G., Wagner, P. E., Wimmer, D., Ye, P. L., Baltensperger, U., Carslaw, K., Kulmala, M., and Curtius, J.: Experimental particle formation rates spanning tropospheric sulfuric acid and ammonia abundances, ion production rates, and temperatures, J Geophys Res-Atmos, 121, 12377-12400, 10.1002/2015jd023908, 2016.

Kürten, A., Li, C., Bianchi, F., Curtius, J., Dias, A., Donahue, N. M., Duplissy, J., Flagan, R. C., Hakala, J., Jokinen, T., Kirkby, J., Kulmala, M., Laaksonen, A., Lehtipalo, K., Makhmutov, V., Onnela, A., Rissanen, M. P., Simon, M., Sipilä, M., Stozhkov, Y., Tröstl, J., Ye, P., and McMurry, P. H.: New particle formation in the sulfuric acid–dimethylamine–water system: reevaluation of CLOUD chamber measurements and comparison to an aerosol nucleation and growth model, Atmos. Chem. Phys., 18, 845-863, 10.5194/acp-18-845-2018, 2018.

Kürten, A.: New particle formation from sulfuric acid and ammonia: nucleation and growth model based on thermodynamics derived from CLOUD measurements for a wide range of conditions, Atmos. Chem. Phys., 19, 5033-5050, 10.5194/acp-19-5033-2019, 2019.

Lee, S. H., Reeves, J. M., Wilson, J. C., Hunton, D. E., Viggiano, A. A., Miller, T. M., Ballenthin, J. O., and Lait, L. R.: Particle formation by ion nucleation in the upper troposphere and lower stratosphere, Science, 301, 1886-1889, DOI 10.1126/science.1087236, 2003.

Lee, S. H., Wilson, J. C., Baumgardner, D., Herman, R. L., Weinstock, E. M., LaFleur, B. G., Kok, G., Anderson, B., Lawson, P., Baker, B., Strawa, A., Pittman, J. V., Reeves, J. M., and Bui, T. P.: New particle formation observed in the tropical/subtropical cirrus clouds, J Geophys Res-Atmos, 109, Artn D2020910.1029/2004jd005033, 2004.

Lovejoy, E. R., Curtius, J., and Froyd, K. D.: Atmospheric ion-induced nucleation of sulfuric acid and water, J Geophys Res-Atmos, 109, Artn D0820410.1029/2003jd004460, 2004.

Luebke, A. E., Afchine, A., Costa, A., Grooss, J. U., Meyer, J., Rolf, C., Spelten, N., Avallone, L. M., Baumgardner, D., and Krämer, M.: The origin of midlatitude ice clouds and the resulting influence on their microphysical properties, Atmospheric Chemistry and Physics, 16, 5793-5809, 10.5194/acp-16-5793-2016, 2016.

Mahnke, C., Weigel, R., Cairo, F., Vernier, J.-P., Afchine, A., Krämer, M., Mitev, V., Matthey, R., Viciani, S., D'Amato, F., Ploeger, F., Deshler, T., and Borrmann, S.: The ATAL within the 2017 Asian Monsoon Anticyclone: Microphysical aerosol properties derived from aircraft-borne in situ measurements, Atmos. Chem. Phys. Discuss., acp-2020-1241 2021.

Manton, M. J.: On the broadening of a droplet distribution by turbulence near cloud base, Q J Roy Meteor Soc, 105, 899-914, 10.1002/qj.49710544613, 1979.

Merikanto, J., Spracklen, D. V., Mann, G. W., Pickering, S. J., and Carslaw, K. S.: Impact of nucleation on global CCN, Atmos Chem Phys, 9, 8601-8616, 10.5194/acp-9-8601-2009, 2009.

Metzger, A., Verheggen, B., Dommen, J., Duplissy, J., Prevot, A. S. H., Weingartner, E., Riipinen, I., Kulmala, M., Spracklen, D. V., Carslaw, K. S., and Baltensperger, U.: Evidence for the role of organics in aerosol particle formation under atmospheric conditions, P Natl Acad Sci USA, 107, 6646-6651, 10.1073/pnas.0911330107, 2010.

Meyer, J., Rolf, C., Schiller, C., Rohs, S., Spelten, N., Afchine, A., Zöger, M., Sitnikov, N., Thornberry, T. D., Rollins, A. W., Bozoki, Z., Tatrai, D., Ebert, V., Kuhnreich, B., Mackrodt, P., Möhler, O., Saathoff, H., Rosenlof, K. H., and Krämer, M.: Two decades of water vapor measurements with the FISH fluorescence hygrometer: a review, Atmos Chem Phys, 15, 8521-8538, 10.5194/acp-15-8521-2015, 2015.

Murphy, D. M., Cziczo, D. J., Froyd, K. D., Hudson, P. K., Matthew, B. M., Middlebrook, A. M., Peltier, R. E., Sullivan, A., Thomson, D. S., and Weber, R. J.: Single-particle mass spectrometry of tropospheric aerosol particles, J Geophys Res-Atmos, 111, Artn D23s32Doi 10.1029/2006jd007340, 2006.

Pan, L. L., Honomichl, S. B., Kinnison, D. E., Abalos, M., Randel, W. J., Bergman, J. W., and Bian, J.: Transport of chemical tracers from the boundary layer to stratosphere associated with the dynamics of the Asian summer monsoon, Journal of Geophysical Research: Atmospheres, 121, 14.159-114.174, 10.1002/2016jd025616, 2016.

Park, M., Randel, W. J., Gettelman, A., Massie, S. T., and Jiang, J. H.: Transport above the Asian summer monsoon anticyclone inferred from Aura Microwave Limb Sounder tracers, J Geophys Res-Atmos, 112, Artn D1630910.1029/2006jd008294, 2007.

Park, M., Randel, W. J., Emmons, L. K., and Livesey, N. J.: Transport pathways of carbon monoxide in the Asian summer monsoon diagnosed from Model of Ozone and Related Tracers (MOZART), J Geophys Res-Atmos, 114, Artn D0830310.1029/2008jd010621, 2009.

Peter, T., Luo, B. P., Wirth, M., Kiemle, C., Flentje, H., Yushkov, V. A., Khattatov, V., Rudakov, V., Thomas, A., Borrmann, S., Toci, G., Mazzinghi, P., Beuermann, J., Schiller, C., Cairo, F., Di Donfrancesco, G., Adriani, A., Volk, C. M., Strom, J., Noone, K., Mitev, V., MacKenzie, R. A., Carslaw,

K. S., Trautmann, T., Santacesaria, V., and Stefanutti, L.: Ultrathin Tropical Tropopause Clouds (UTTCs): I. Cloud morphology and occurrence, Atmos. Chem. Phys., 3, 1083-1091, 10.5194/acp-3-1083-2003, 2003.

Ploeger, F., Günther, G., Konopka, P., Fueglistaler, S., Müller, R., Hoppe, C., Kunz, A., Spang, R., Grooss, J. U., and Riese, M.: Horizontal water vapor transport in the lower stratosphere from subtropics to high latitudes during boreal summer, J Geophys Res-Atmos, 118, 8111-8127, 10.1002/jgrd.50636, 2013.

Politovich, M. K., and Cooper, W. A.: Variability of the Supersaturation in Cumulus Clouds, Journal of the Atmospheric Sciences, 45, 1651-1664, 10.1175/1520-0469(1988)045<1651:votsic>2.0.co;2, 1988.

Pöschl, U., Canagaratna, M., Jayne, J. T., Molina, L. T., Worsnop, D. R., Kolb, C. E., and Molina, M. J.: Mass Accommodation Coefficient of H_2SO_4 Vapor on Aqueous Sulfuric Acid Surfaces and Gaseous Diffusion Coefficient of H_2SO_4 in N_2/H_2O, The Journal of Physical Chemistry A, 102, 10082-10089, 10.1021/jp982809s, 1998.

Pruppacher, H. R., and Klett, J. D.: Microphysics of Clouds and Precipitation: Reprinted 1980, Springer Science & Business Media, 2012.

Radke, L. F., and Hobbs, P. V.: Humidity and Particle Fields around Some Small Cumulus Clouds, Journal of the Atmospheric Sciences, 48, 1190-1193, Doi 10.1175/1520-0469(1991)048<1190:Hapfas>2.0.Co;2, 1991.

Randel, W. J., and Park, M.: Deep convective influence on the Asian summer monsoon anticyclone and associated tracer variability observed with Atmospheric Infrared Sounder (AIRS), J Geophys Res-Atmos, 111, Artn D1231410.1029/2005jd006490, 2006.

Ranjithkumar, A., Gordon, H., Williamson, C., Rollins, A., Pringle, K., Kupc, A., Abraham, N. L., Brock, C., and Carslaw, K.: Constraints on global aerosol number concentration, SO2 and condensation sink in UKESM1 using ATom measurements, Atmos. Chem. Phys., 21, 4979-5014, 10.5194/acp-21-4979-2021, 2021.

Riccobono, F., Schobesberger, S., Scott, C. E., Dommen, J., Ortega, I. K., Rondo, L., Almeida, J., Amorim, A., Bianchi, F., Breitenlechner, M., David, A., Downard, A., Dunne, E. M., Duplissy, J., Ehrhart, S., Flagan, R. C., Franchin, A., Hansel, A., Junninen, H., Kajos, M., Keskinen, H., Kupc, A., Kürten, A., Kvashin, A. N., Laaksonen, A., Lehtipalo, K., Makhmutov, V., Mathot, S., Nieminen, T., Onnela, A., Petaja, T., Praplan, A. P., Santos, F. D., Schallhart, S., Seinfeld, J. H., Sipila, M., Spracklen, D. V., Stozhkov, Y., Stratmann, F., Tome, A., Tsagkogeorgas, G., Vaattovaara, P., Viisanen, Y., Vrtala, A., Wagner, P. E., Weingartner, E., Wex, H., Wimmer, D., Carslaw, K. S., Curtius, J., Donahue, N. M., Kirkby, J., Kulmala, M., Worsnop, D. R., and Baltensperger, U.: Oxidation Products of Biogenic Emissions Contribute to Nucleation of Atmospheric Particles, Science, 344, 717-721, 10.1126/science.1243527, 2014.

Schulz, C., Schneider, J., Holanda, B. A., Appel, O., Costa, A., de Sa, S. S., Dreiling, V., Fütterer, D., Jurkat-Witschas, T., Klimach, T., Knote, C., Krämer, M., Martin, S. T., Mertes, S., Pöhlker, M. L., Sauer, D., Voigt, C., Walser, A., Weinzierl, B., Ziereis, H., Zöger, M., Andreae, M. O., Artaxo, P., Machado, L. A. T., Pöschl, U., Wendisch, M., and Borrmann, S.: Aircraft-based observations of isoprene-epoxydiol-derived secondary organic aerosol (IEPOX-SOA) in the tropical upper troposphere over the Amazon region, Atmos Chem Phys, 18, 14979-15001, 10.5194/acp-18-14979-2018, 2018.

Schumann, U., Kiemle, C., Schlager, H., Weigel, R., Borrmann, S., D'Amato, F., Krämer, M., Matthey, R., Protat, A., Voigt, C., and Volk, C. M.: Long-lived contrails and convective cirrus above the tropical tropopause, Atmos. Chem. Phys., 17, 2311-2346, 10.5194/acp-17-2311-2017, 2017.

Sokolov, L., and Lepuchov, B.: Protocol of interaction between Unit for Connection with Scientific Equipment (UCSE) and on-board scientific equipment of Geophysica aircraft (Second edition), Myasishchev Design Bureau (MDB), 1998.

Speidel, M., Nau, R., Arnold, F., Schlager, H., and Stohl, A.: Sulfur dioxide measurements in the lower, middle and upper troposphere: Deployment of an aircraft-based chemical ionization mass spectrometer with permanent in-flight calibration, Atmos Environ, 41, 2427-2437, 10.1016/j.atmosenv.2006.07.047, 2007.

Spracklen, D. V., Carslaw, K. S., Kulmala, M., Kerminen, V. M., Mann, G. W., and Sihto, S. L.: The contribution of boundary layer nucleation events to total particle concentrations on regional and global scales, Atmos Chem Phys, 6, 5631-5648, DOI 10.5194/acp-6-5631-2006, 2006.

Spreitzer, E. J., Marschalik, M. P., and Spichtinger, P.: Subvisible cirrus clouds - a dynamical system approach, Nonlinear Proc Geoph, 24, 307-328, 10.5194/npg-24-307-2017, 2017.

Tang, M. J., Cox, R. A., and Kalberer, M.: Compilation and evaluation of gas phase diffusion coefficients of reactive trace gases in the atmosphere: volume 1. Inorganic compounds, Atmos. Chem. Phys., 14, 9233-9247, 10.5194/acp-14-9233-2014, 2014.

Thomas, A., Borrmann, S., Kiemle, C., Cairo, F., Volk, M., Beuermann, J., Lepuchov, B., Santacesaria, V., Matthey, R., Rudakov, V., Yushkov, V., MacKenzie, A. R., and Stefanutti, L.: In situ measurements of background aerosol and subvisible cirrus in the tropical tropopause region, Journal of Geophysical Research: Atmospheres, 107, AAC 8-1-AAC 8-14, 10.1029/2001jd001385, 2002.

Tsagkogeorgas, G., Roldin, P., Duplissy, J., Rondo, L., Tröstl, J., Slowik, J. G., Ehrhart, S., Franchin, A., Kürten, A., Amorim, A., Bianchi, F., Kirkby, J., Petäjä, T., Baltensperger, U., Boy, M., Curtius, J., Flagan, R. C., Kulmala, M., Donahue, N. M., and Stratmann, F.: Evaporation of sulfate aerosols at low relative humidity, Atmos. Chem. Phys., 17, 8923-8938, 10.5194/acp-17-8923-2017, 2017.

Twohy, C. H., Clement, C. F., Gandrud, B. W., Weinheimer, A. J., Campos, T. L., Baumgardner, D., Brune, W. H., Faloona, I., Sachse, G. W., Vay, S. A., and Tan, D.: Deep convection as a source of new particles in the midlatitude upper troposphere, J Geophys Res-Atmos, 107, Artn 456010.1029/2001jd000323, 2002.

Ueyama, R., Jensen, E. J., Pfister, L., Krämer, M., Afchine, A., and Schoeberl, M.: Impact of Convectively Detrained Ice Crystals on the Humidity of the Tropical Tropopause Layer in Boreal Winter, Journal of Geophysical Research: Atmospheres, 125, e2020JD032894, 10.1029/2020JD032894, 2020.

Vehkamäki, H., Kulmala, M., Napari, I., Lehtinen, K. E. J., Timmreck, C., Noppel, M., and Laaksonen, A.: An improved parameterization for sulfuric acid–water nucleation rates for tropospheric and stratospheric conditions, Journal of Geophysical Research: Atmospheres, 107, AAC 3-1-AAC 3-10, 10.1029/2002jd002184, 2002.

Venzac, H., Sellegri, K., Laj, P., Villani, P., Bonasoni, P., Marinoni, A., Cristofanelli, P., Calzolari, F., Fuzzi, S., Decesari, S., Facchini, M. C., Vuillermoz, E., and Verza, G. P.: High frequency new particle formation in the Himalayas, P Natl Acad Sci USA, 105, 15666-15671, 10.1073/pnas.0801355105, 2008.

Vernier, J.-P., Fairlie, T. D., Deshler, T., Ratnam, M. V., Gadhavi, H., Kumar, B. S., Natarajan, M., Pandit, A. K., Raj, S. T. A., Kumar, A. H., Jayaraman, A., Singh, A. K., Rastogi, N., Sinha, P. R., Kumar, S., Tiwari, S., Wegner, T., Baker, N., Vignelles, D., Stenchikov, G., Shevchenko, I., Smith, J., Bedka, K., Kesarkar, A., Singh, V., Bhate, J., Ravikiran, V., Rao, M. D., Ravindrababu, S., Patel, A., Vernier, H., Wienhold, F. G., Liu, H., Knepp, T. N., Thomason, L., Crawford, J., Ziemba, L., Moore, J., Crumeyrolle, S., Williamson, M., Berthet, G., Jégou, F., and Renard, J.-B.: BATAL: The Balloon Measurement Campaigns of the Asian Tropopause Aerosol Layer, B Am Meteorol Soc, 99, 955-973, 10.1175/bams-d-17-0014.1, 2018.

Vernier, J. P., Thomason, L. W., and Kar, J.: CALIPSO detection of an Asian tropopause aerosol layer, Geophys Res Lett, 38, Artn L0780410.1029/2010gl046614, 2011.

Vernier, J. P., Fairlie, T. D., Natarajan, M., Wienhold, F. G., Bian, J., Martinsson, B. G., Crumeyrolle, S., Thomason, L. W., and Bedka, K. M.: Increase in upper tropospheric and lower stratospheric aerosol levels and its potential connection with Asian pollution, J Geophys Res-Atmos, 120, 1608-1619, 10.1002/2014jd022372, 2015.

Viciani, S., D'Amato, F., Mazzinghi, P., Castagnoli, F., Toci, G., and Werle, P.: A cryogenically operated laser diode spectrometer for airborne measurement of stratospheric trace gases, Applied Physics B, 90, 581-592, 10.1007/s00340-007-2885-2, 2008.

Viciani, S., Montori, A., Chiarugi, A., and D'Amato, F.: A Portable Quantum Cascade Laser Spectrometer for Atmospheric Measurements of Carbon Monoxide, Sensors, 18, 2380, doi:10.3390/s18072380, 2018.

Vogel, B., Günther, G., Müller, R., Grooss, J. U., Hoor, P., Krämer, M., Müller, S., Zahn, A., and Riese, M.: Fast transport from Southeast Asia boundary layer sources to northern Europe: rapid uplift in typhoons and eastward eddy shedding of the Asian monsoon anticyclone, Atmos Chem Phys, 14, 12745-12762, 10.5194/acp-14-12745-2014, 2014.

Vogel, B., Müller, R., Günther, G., Spang, R., Hanumanthu, S., Li, D., Riese, M., and Stiller, G. P.: Lagrangian simulations of the transport of young air masses to the top of the Asian monsoon anticyclone and into the tropical pipe, Atmos Chem Phys, 19, 6007-6034, 10.5194/acp-19-6007-2019, 2019.

Waddicor, D. A., Vaughan, G., Choularton, T. W., Bower, K. N., Coe, H., Gallagher, M., Williams, P. I., Flynn, M., Volz-Thomas, A., Patz, H. W., Isaac, P., Hacker, J., Arnold, F., Schlager, H., and Whiteway, J. A.: Aerosol observations and growth rates downwind of the anvil of a deep tropical thunderstorm, Atmos Chem Phys, 12, 6157-6172, 10.5194/acp-12-6157-2012, 2012.

Wang, M., Kong, W., Marten, R., He, X.-C., Chen, D., Pfeifer, J., Heitto, A., Kontkanen, J., Dada, L., Kürten, A., Yli-Juuti, T., Manninen, H. E., Amanatidis, S., Amorim, A., Baalbaki, R., Baccarini, A., Bell, D. M., Bertozzi, B., Bräkling, S., Brilke, S., Murillo, L. C., Chiu, R., Chu, B., De Menezes, L.-P., Duplissy, J., Finkenzeller, H., Carracedo, L. G., Granzin, M., Guida, R., Hansel, A., Hofbauer, V., Krechmer, J., Lehtipalo, K., Lamkaddam, H., Lampimäki, M., Lee, C. P., Makhmutov, V., Marie, G., Mathot, S., Mauldin, R. L., Mentler, B., Müller, T., Onnela, A., Partoll, E., Petäjä, T., Philippov, M., Pospisilova, V., Ranjithkumar, A., Rissanen, M., Rörup, B., Scholz, W., Shen, J., Simon, M., Sipilä, M., Steiner, G., Stolzenburg, D., Tham, Y. J., Tomé, A., Wagner, A. C., Wang, D. S., Wang, Y., Weber, S. K., Winkler, P. M., Wlasits, P. J., Wu, Y., Xiao, M., Ye, Q., Zauner-Wieczorek, M., Zhou, X., Volkamer, R., Riipinen, I., Dommen, J., Curtius, J., Baltensperger, U., Kulmala, M., Worsnop, D. R., Kirkby, J., Seinfeld, J. H., El-Haddad, I., Flagan, R. C., and Donahue, N. M.: Rapid growth of new atmospheric particles by nitric acid and ammonia condensation, Nature, 581, 184-189, 10.1038/s41586-020-2270-4, 2020.

Weber, R. J., Clarke, A. D., Litchy, M., Li, J., Kok, G., Schillawski, R. D., and McMurry, P. H.: Spurious aerosol measurements when sampling from aircraft in the vicinity of clouds, Journal of Geophysical Research: Atmospheres, 103, 28337-28346, 10.1029/98jd02086, 1998.

Wehner, B., Werner, F., Ditas, F., Shaw, R. A., Kulmala, M., and Siebert, H.: Observations of new particle formation in enhanced UV irradiance zones near cumulus clouds, Atmos Chem Phys, 15, 11701-11711, 10.5194/acp-15-11701-2015, 2015.

Weigel, R., Hermann, M., Curtius, J., Voigt, C., Walter, S., Bottger, T., Lepukhov, B., Belyaev, G., and Borrmann, S.: Experimental characterization of the COndensation PArticle counting System for high altitude aircraft-borne application, Atmos Meas Tech, 2, 243-258, 10.5194/amt-2-243-2009, 2009.

Weigel, R., Borrmann, S., Kazil, J., Minikin, A., Stohl, A., Wilson, J. C., Reeves, J. M., Kunkel, D., de Reus, M., Frey, W., Lovejoy, E. R., Volk, C. M., Viciani, S., D'Amato, F., Schiller, C., Peter, T., Schlager, H., Cairo, F., Law, K. S., Shur, G. N., Belyaev, G. V., and Curtius, J.: In situ observations of new particle formation in the tropical upper troposphere: the role of clouds and the nucleation mechanism, Atmos Chem Phys, 11, 9983-10010, 10.5194/acp-11-9983-2011, 2011.

Weigel, R., Volk, C. M., Kandler, K., Hosen, E., Gunther, G., Vogel, B., Grooss, J. U., Khaykin, S., Belyaev, G. V., and Borrmann, S.: Enhancements of the refractory submicron aerosol fraction in the Arctic polar vortex: feature or exception?, Atmos Chem Phys, 14, 12319-12342, DOI 10.5194/acp-14-12319-2014, 2014.

Weigel, R., Mahnke, C., Baumgartner, M., Dragoneas, A., Vogel, B., Ploeger, F., Viciani, S., D'Amato, F., Bucci, S., Legras, B., Luo, B., Belyaev, G. V., and Borrmann, S.: In-Situ observation of New Particle Formation (NPF) in the tropical tropopause layer of the 2017 Asian Monsoon Anticyclone: Part I - summary of StratoClim results Atmos. Chem. Phys. Discuss., acp-2020-1158, 2021a.

Weigelt, A., Hermann, M., van Velthoven, P. F. J., Brenninkmeijer, C. A. M., Schlaf, G., Zahn, A., and Wiedensohler, A.: Influence of clouds on aerosol particle number concentrations in the upper troposphere, J Geophys Res-Atmos, 114, Artn D0120410.1029/2008jd009805, 2009.

Wernli, H., Boettcher, M., Joos, H., Miltenberger, A. K., and Spichtinger, P.: A trajectory-based classification of ERA-Interim ice clouds in the region of the North Atlantic storm track, Geophys Res Lett, 43, 6657-6664, 10.1002/2016gl068922, 2016.

Williamson, C. J., Kupc, A., Axisa, D., Bilsback, K. R., Bui, T., Campuzano-Jost, P., Dollner, M., Froyd, K. D., Hodshire, A. L., Jimenez, J. L., Kodros, J. K., Luo, G., Murphy, D. M., Nault, B. A., Ray, E. A., Weinzierl, B., Wilson, J. C., Yu, F., Yu, P., Pierce, J. R., and Brock, C. A.: A large source of cloud condensation nuclei from new particle formation in the tropics, Nature, 574, 399-403, 10.1038/s41586-019-1638-9, 2019.

WMO: International Meteorological Tables, WMO-No.188.TP97, edited by: Letestu, S., Secretariat of the World Meteorological Organization, Geneva, Switzerland, 1966.

Yu, P. F., Toon, O. B., Neely, R. R., Martinsson, B. G., and Brenninkmeijer, C. A. M.: Composition and physical properties of the Asian Tropopause Aerosol Layer and the North American Tropospheric Aerosol Layer, Geophys Res Lett, 42, 2540-2546, 10.1002/2015gl063181, 2015.

Zöger, M., Afchine, A., Eicke, N., Gerhards, M. T., Klein, E., McKenna, D. S., Morschel, U., Schmidt, U., Tan, V., Tuitjer, F., Woyke, T., and Schiller, C.: Fast in situ stratospheric hygrometers: A new family of balloon-borne and airborne Lyman alpha photofragment fluorescence hygrometers, J Geophys Res-Atmos, 104, 1807-1816, Doi 10.1029/1998jd100025, 1999.

Figure captions

Figure 1: The flight patterns of the M-55 *Geophysica* during StratoClim 2017 over the Indian subcontinent. New particle formation (NPF) encountered in clear air along the flight tracks are indicated by orange colour in the main panel a). All NPF events coinciding with the detection of cloud (ice) particles are coloured in blue. The general perspective, b), exhibits the patterns of the eight StratoClim flights over Nepal, North - East India, Bangladesh, and the Bay of Bengal. For more details, see Table 1.

Figure 2: Number concentrations (1 Hz - resolved) of aerosol particles in the nucleation-mode size range (N_{nm}) and of cloud (ice) particles (N_{ice}) of the eight StratoClim flights compiled in one time series ranging from 03:30 (UTC) to 12:30 (UTC). Kathmandu's (Nepal) local noontime is indicated by the vertical orange line (corresponding to 06:15 UTC, or 22500 seconds of day, UTC). Panel b): incidences of concentrations N_{nm} exceeding 500 cm^{-3}, 1000 cm^{-3}, and 5000 cm^{-3} within 15 minute time intervals. Data points of N_{nm} in black whenever N_{ice} (cyan) equals zero, otherwise N_{nm} is coloured in red. The blue dashed line (Panel c) indicates the median of N_{ice} (0.031 cm^{-3}) over all cloud particle detections during StratoClim 2017 (Krämer et al., 2020).

Figure 3: Vertical profiles of the mixing ratio (1 Hz - resolved) of aerosols in the nucleation-mode size range (n_{nm}) versus the potential temperature (θ). a): all data separated concerning coincident detection of cloud (ice) particles (black: $N_{\mathrm{ice}} = 0\ \mathrm{cm}^{-3}$, red: $N_{\mathrm{ice}} > 0\ \mathrm{cm}^{-3}$) and b): all data coloured in reference to the flight date, c): exclusively for $N_{\mathrm{ice}} > 0\ \mathrm{cm}^{-3}$, and d): when $N_{\mathrm{ice}} = 0\ \mathrm{cm}^{-3}$. In the panels at the bottom (e and f), in-cloud and clear-air measurements are distinguished as in intermediate panels (c and d) and coloured with reference to carbon monoxide (CO) mixing ratios.

Figure 4: Histograms of the occurrence frequency of number concentrations N_{nm} of all NPF detections (1 Hz - resolved) throughout StratoClim 2017. a): all data of N_{nm} in general (black) and separated concerning coincident detection of cloud (ice) particles in the diameter size range $3\ \mu\mathrm{m} < d_{\mathrm{p}} < 937\ \mu\mathrm{m}$ (green: $N_{\mathrm{ice}} = N_{3\text{-}937\mu\mathrm{m}} = 0\ \mathrm{cm}^{-3}$, red: $N_{\mathrm{ice}} > 0\ \mathrm{cm}^{-3}$). The sum of the green and red curve yield the black curve, the vertical bars of which represent the square root of counts. b): relative occurrence frequency of N_{nm} for in-cloud NPF (if detected coincidently with $N_{\mathrm{ice}} > 0\ \mathrm{cm}^{-3}$) normalised with respect to all NPF detections, i.e. the ratio of the absolute occurrence frequencies (in red and black in Panel a). c): relative occurrence frequency of N_{nm} for in-cloud NPF, if detected coincidently with various N_{ice} levels, which were normalised with respect to those NPF detections with $N_{\mathrm{ice}} > 0\ \mathrm{cm}^{-3}$, (in red, Panel b).

Figure 5: StratoClim 2017 data of the total number concentration N_{10} together with coincident detections of N_{ice} (i.e. $N_{3\text{-}937\mu\mathrm{m}}$) by the NIXE-CAPS. The vertical bars represent the standard deviation over the averaging periods. Data points are colour-coded in a) with reference to *IWC*. b): NPF encounters (orange) throughout the averaging period (otherwise grey). Blue-shaded areas in both panels indicate the range of most of the data points provided by de Reus et al. (2009). Reference lines for concentration ratios of 1 : 300 and 1 : 30 000 (as in de Reus et al. (2009)), and here additionally for 1 : 500 000 and 1 : 5 000 000 are provided.

Figure 6: NPF in the *IWC* - *T* parameter space (cf. Krämer et al. (2016)): measured ice water content (*IWC*) coincidently detected with COPAS data as a function of ambient air temperature throughout StratoClim 2017 (1 Hz - resolved). Data points are colour-coded referring to (a) the

detected mixing ratios of nucleation-mode particles, n_{nm}, (b) the total mixing ratio n_6, and (c) the carbon monoxide (CO) mixing ratio. Note: in (a), the data points are grey if data of $n_{6\text{-}15}$ are available, while colours are apportioned only to those n_{nm} (i.e. $n_{6\text{-}15}$) complying with the NPF criterion. Generally, the black lines represent the median (solid) and the upper-/lowermost bounds (dashed) of the core *IWC* band, respectively, as obtained from earlier measurements at other locations (Krämer et al. (2016)).

Figure 7: Concentrations of in-cloud detected nucleation-mode aerosols (N_{nm}) in 1 Hz – resolution as a function of the mean inter-crystal distance, *ICD*, between encountered cloud (ice) particles colour-coded with reference to (a) the number concentration of cloud ice particles, (b) to the *IWC*, and (c) to the mean ice particles' radius.

Figure 8: Concentrations of nucleation-mode aerosols (N_{nm}) in 1 Hz – resolution as a function of the cloud (ice) particles' integral radius, $IR = \overline{r_{\mathrm{ice}}} \cdot N_{\mathrm{ice}}$ colour-coded in correspondence to detected ice water content (*IWC*, panel a) and to measured CO mixing ratio (b); in the absence of CO values the data points are blackened. The diagonal, grey-coloured bars indicate a limiting range, beyond which the probability of NPF observations decreases, with two exceptional encounters of very recent or just proceeding NPF (see text for details).

Figure B- 1: Simulated change of the H_2SO_4 vapour's saturation ratio as a function of time due to the presence of entirely H_2SO_4 - coated ice particle surfaces of various sizes and number concentrations. a): particles with radii $r_p = 1$ µm, b): $r_p = 10$ µm, c): $r_p = 100$ µm. Overall, this simulation covers a range of integral radii *IR* (= $\overline{\boldsymbol{r}_{\mathrm{ice}}} \cdot \boldsymbol{N}_{\mathbf{ice}}$) from 0.01 to 10 µm cm^{-3}. Note: a cloud (ice) particle is assumed as coated with H_2SO_4 (consistent with Bogdan et al. (2006); Bogdan et al. (2013)).

Figures

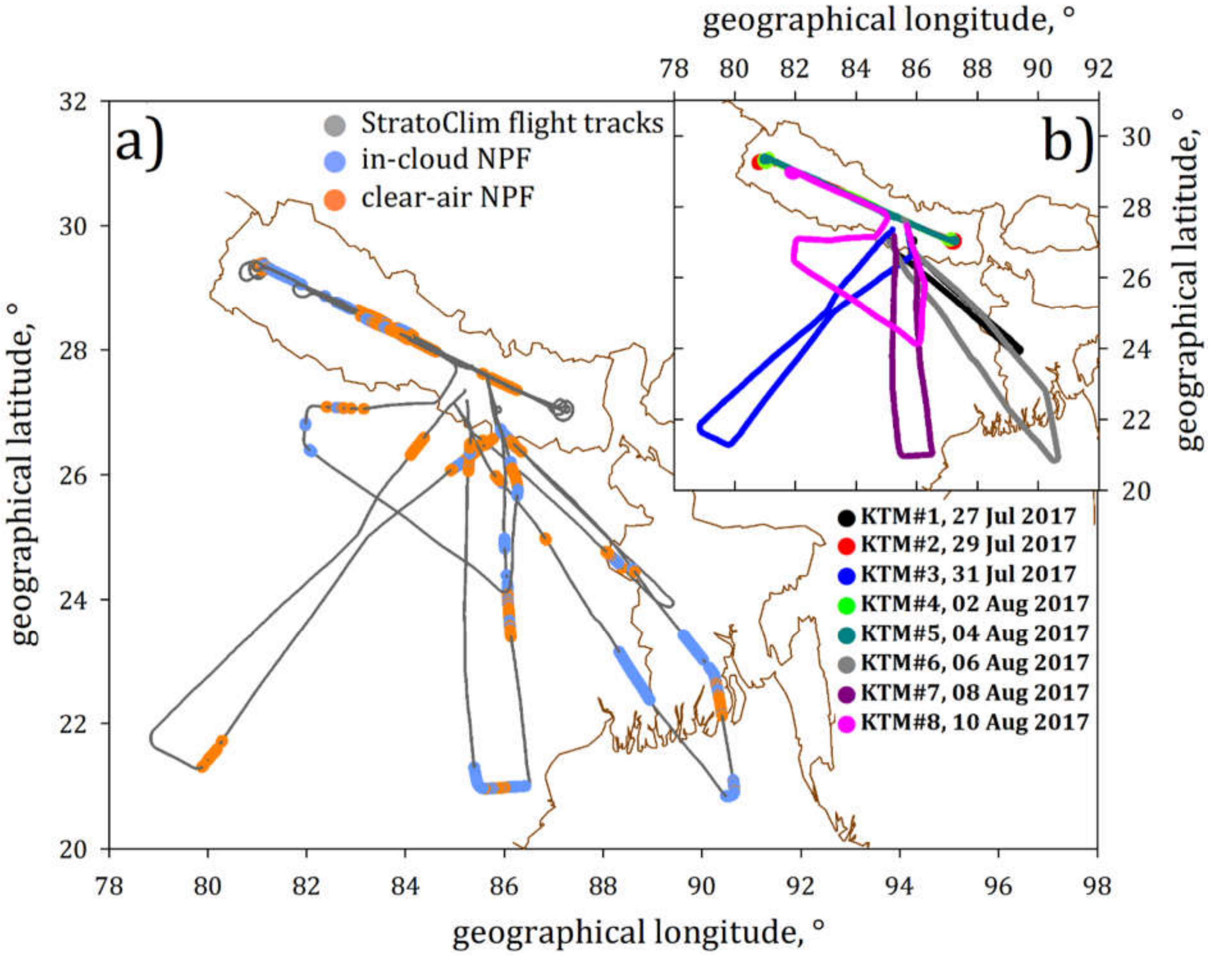

Figure 1

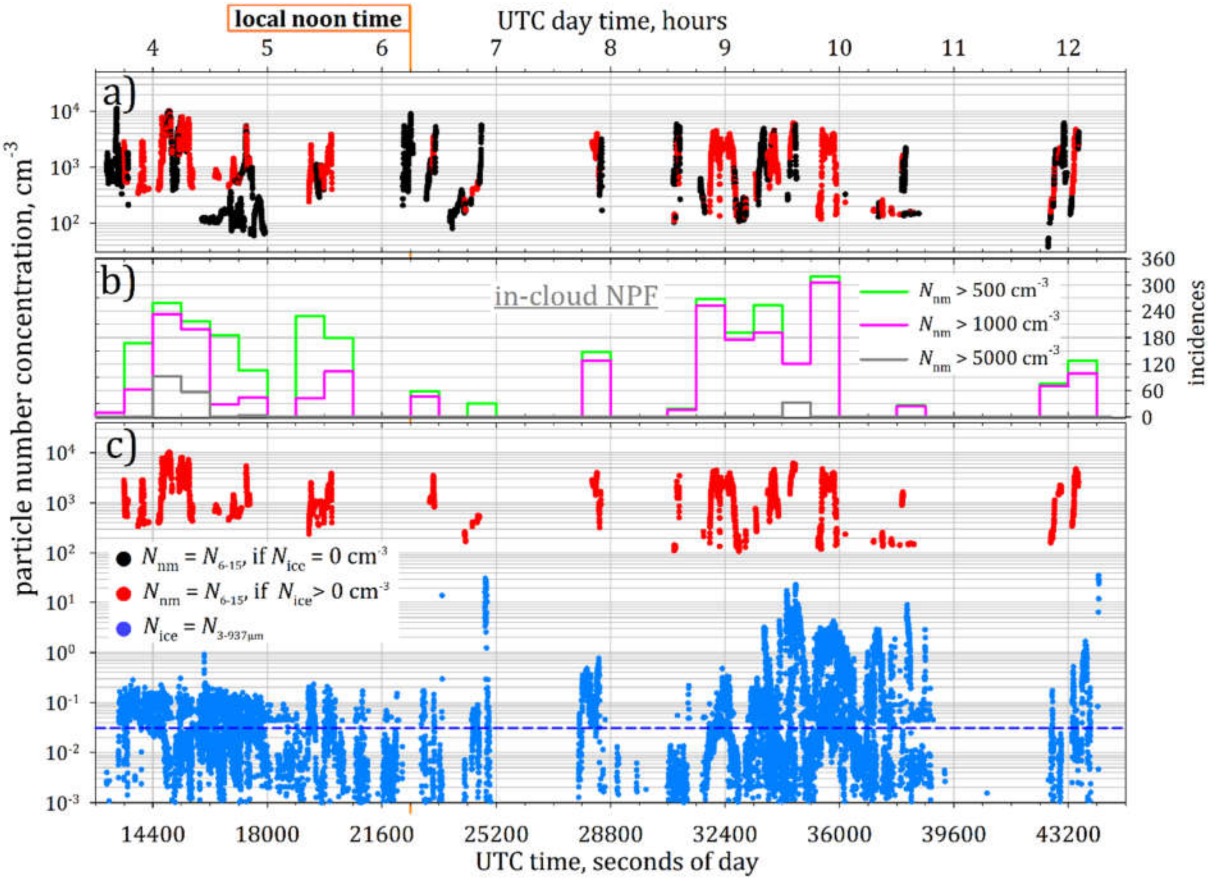
local noon time
UTC day time, hours
4
5
6
7
8
9
10
11
12
a)
b)
c)
10^4
10^3
10^2
10^1
10^0
10^{-1}
10^{-2}
10^{-3}
particle number concentration, cm^{-3}
in-cloud NPF
$N_{nm} > 500\ cm^{-3}$
$N_{nm} > 1000\ cm^{-3}$
$N_{nm} > 5000\ cm^{-3}$
360
300
240
180
120
60
0
incidences
$N_{nm} = N_{6\text{-}15}$, if $N_{ice} = 0\ cm^{-3}$
$N_{nm} = N_{6\text{-}15}$, if $N_{ice} > 0\ cm^{-3}$
$N_{ice} = N_{3\text{-}937\mu m}$
14400
18000
21600
25200
28800
32400
36000
39600
43200
UTC time, seconds of day

Figure 2

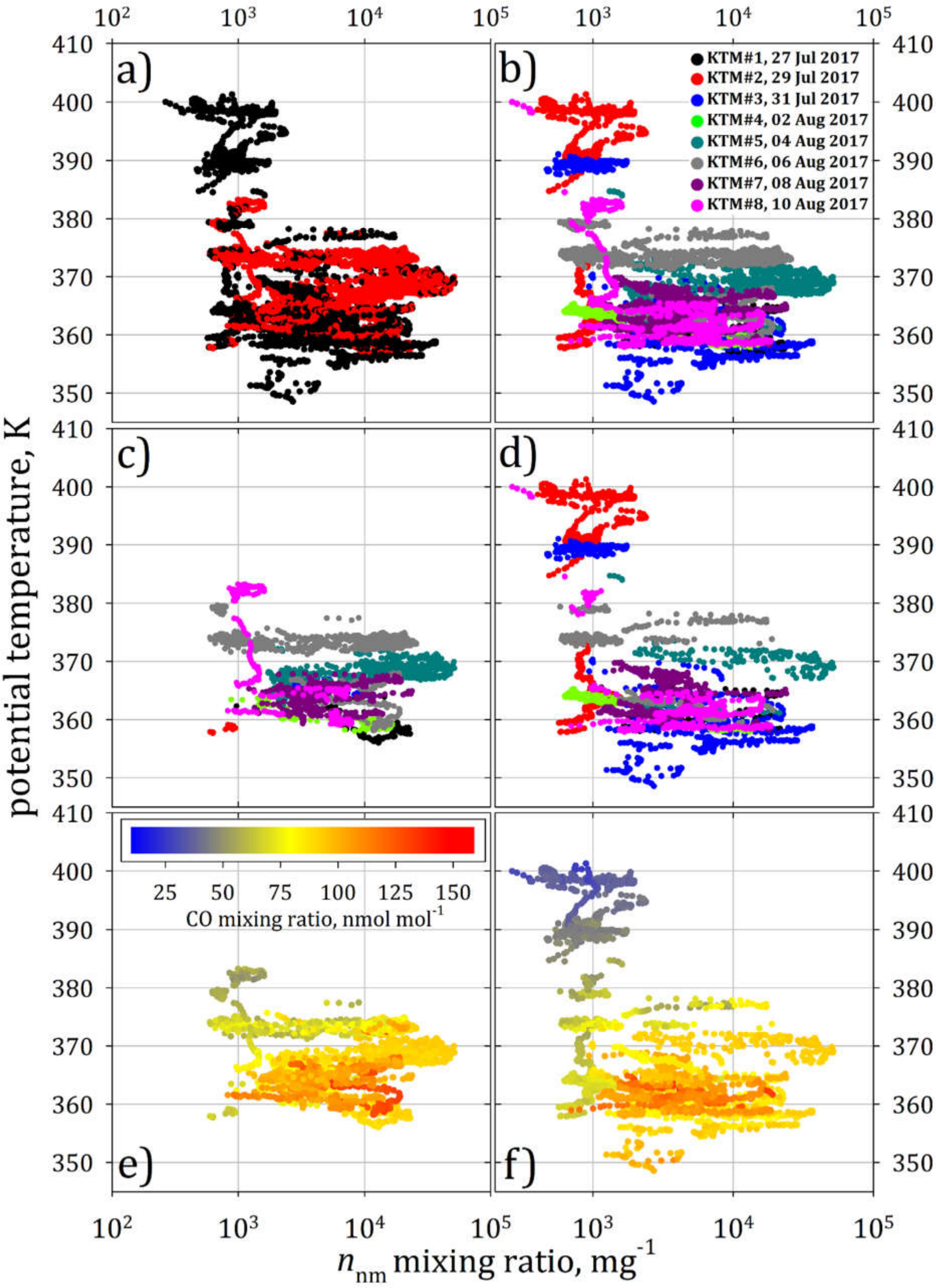
a)
b)
c)
d)
e)
f)
10²
10³
10⁴
10⁵
410
400
390
380
370
360
350
potential temperature, K
KTM#1, 27 Jul 2017
KTM#2, 29 Jul 2017
KTM#3, 31 Jul 2017
KTM#4, 02 Aug 2017
KTM#5, 04 Aug 2017
KTM#6, 06 Aug 2017
KTM#7, 08 Aug 2017
KTM#8, 10 Aug 2017
25
50
75
100
125
150
CO mixing ratio, nmol mol⁻¹
n_{nm} mixing ratio, mg⁻¹

Figure 3

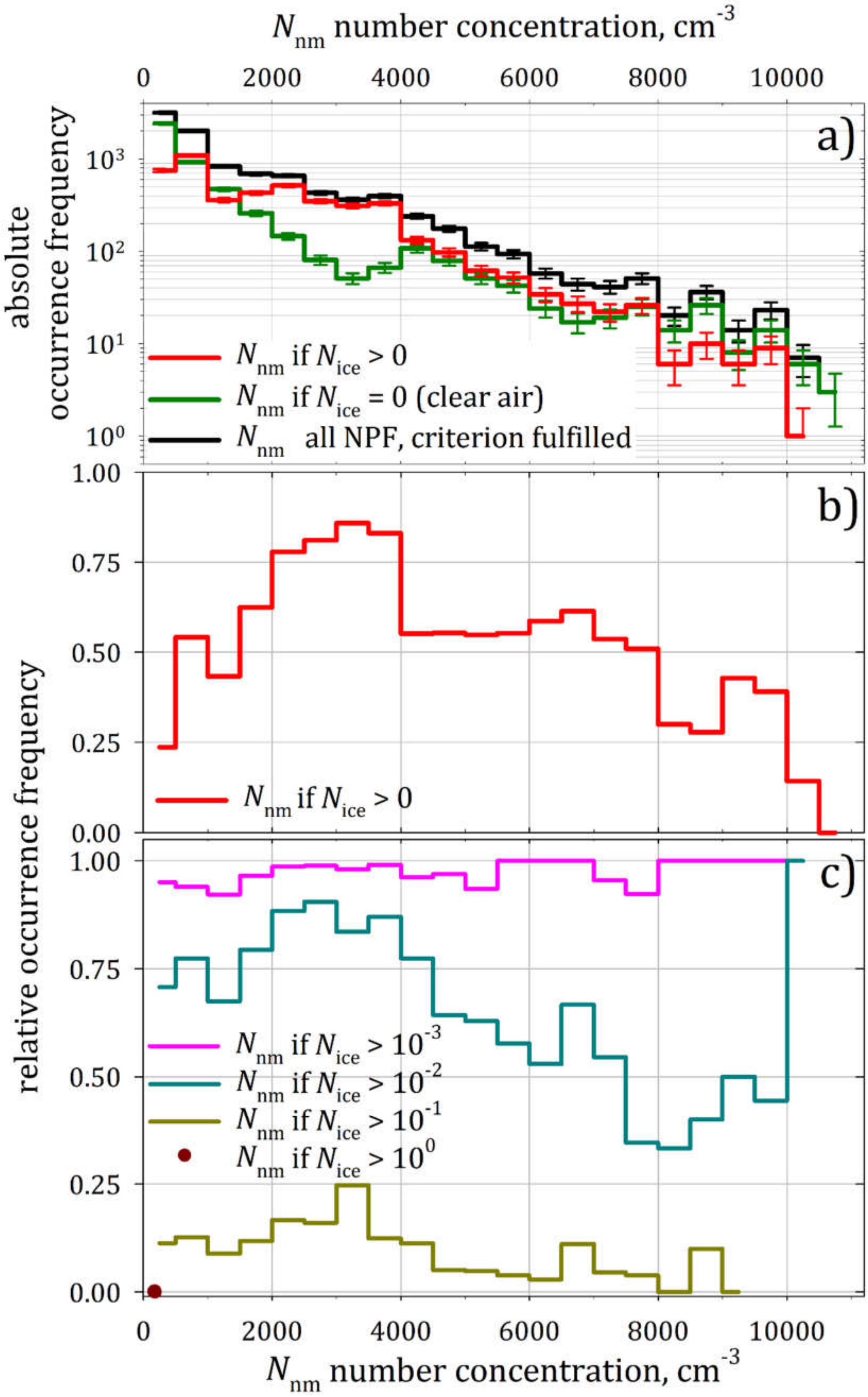
N_{nm} number concentration, cm^{-3}
0
2000
4000
6000
8000
10000
a)
absolute occurrence frequency
10^3
10^2
10^1
10^0
N_{nm} if $N_{ice} > 0$
N_{nm} if $N_{ice} = 0$ (clear air)
N_{nm} all NPF, criterion fulfilled
b)
1.00
0.75
0.50
0.25
0.00
N_{nm} if $N_{ice} > 0$
relative occurrence frequency
c)
N_{nm} if $N_{ice} > 10^{-3}$
N_{nm} if $N_{ice} > 10^{-2}$
N_{nm} if $N_{ice} > 10^{-1}$
N_{nm} if $N_{ice} > 10^{0}$

Figure 4

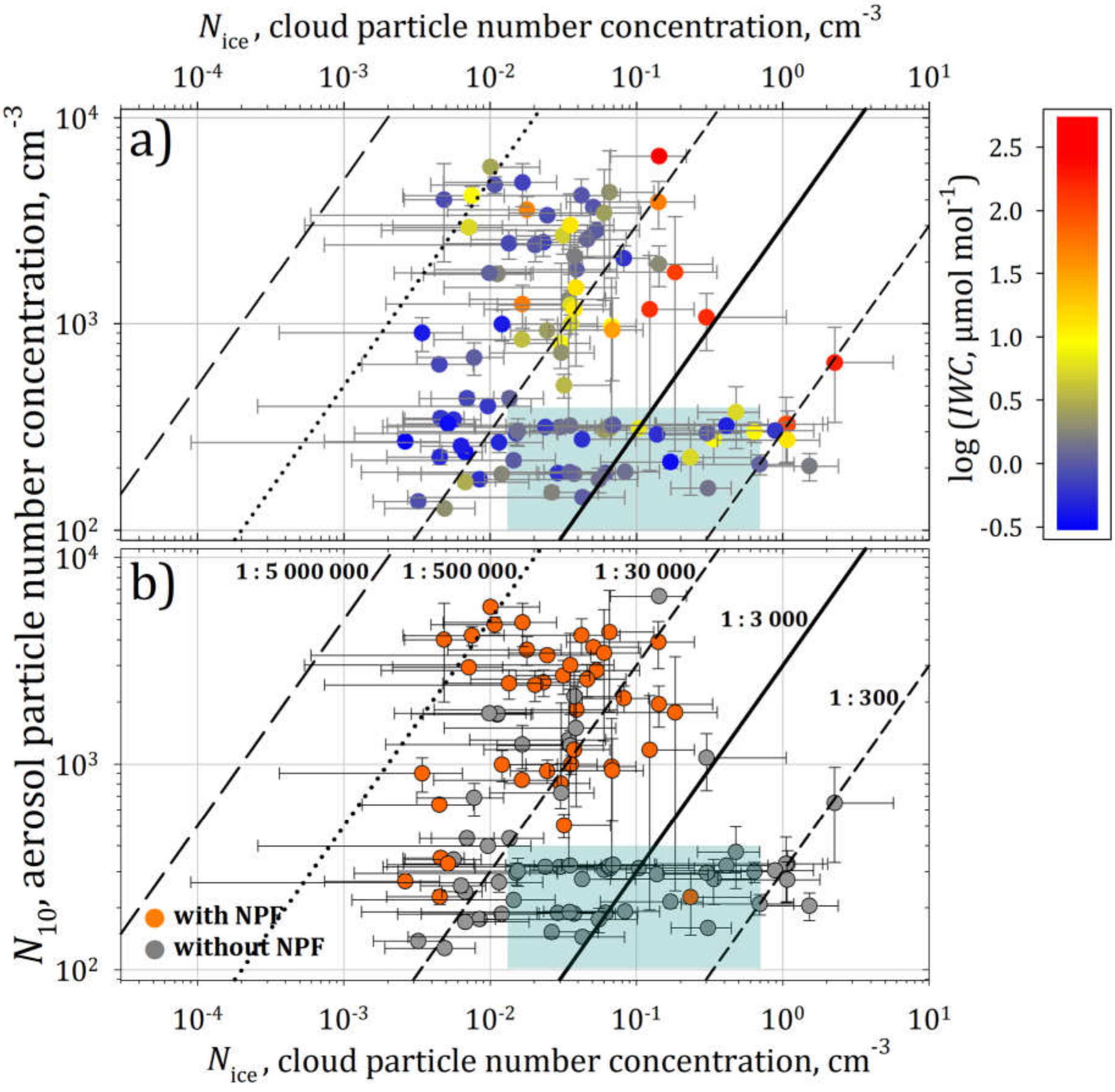

N_{ice}, cloud particle number concentration, cm^{-3}
10^{-4}
10^{-3}
10^{-2}
10^{-1}
10^{0}
10^{1}
N_{10}, aerosol particle number concentration, cm^{-3}
10^{4}
10^{3}
10^{2}
a)
b)
log (IWC, µmol mol^{-1})
2.5
2.0
1.5
1.0
0.5
0.0
-0.5
1 : 5 000 000
1 : 500 000
1 : 30 000
1 : 3 000
1 : 300
● with NPF
● without NPF

Figure 5

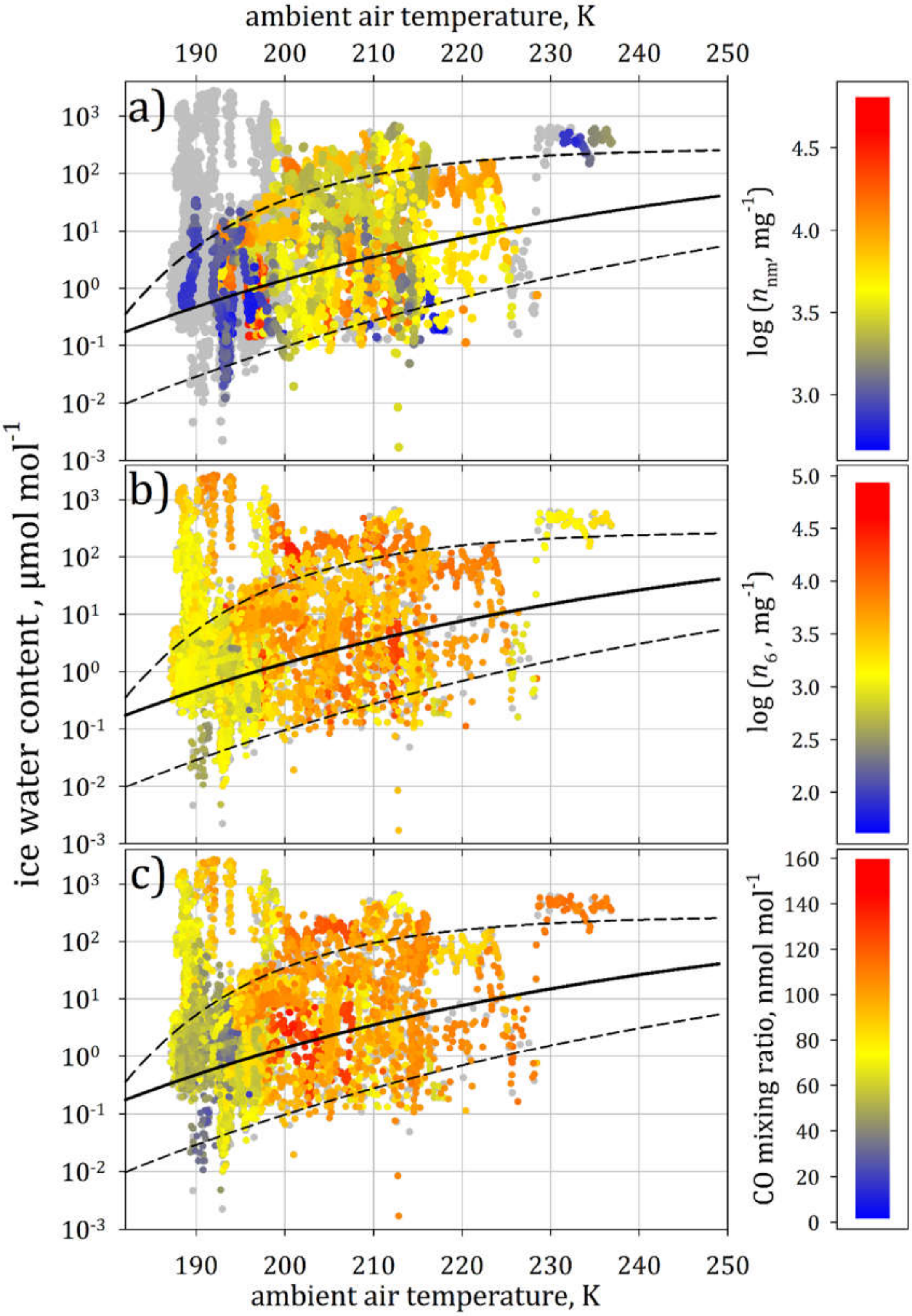
ambient air temperature, K
190
200
210
220
230
240
250
a)
b)
c)
ice water content , µmol mol^{-1}
10^3
10^2
10^1
10^0
10^{-1}
10^{-2}
10^{-3}
log (n_{nm}, mg^{-1})
4.5
4.0
3.5
3.0
log (n_6 , mg^{-1})
5.0
4.5
4.0
3.5
3.0
2.5
2.0
CO mixing ratio, nmol mol^{-1}
160
140
120
100
80
60
40
20
0
ambient air temperature, K

Figure 6

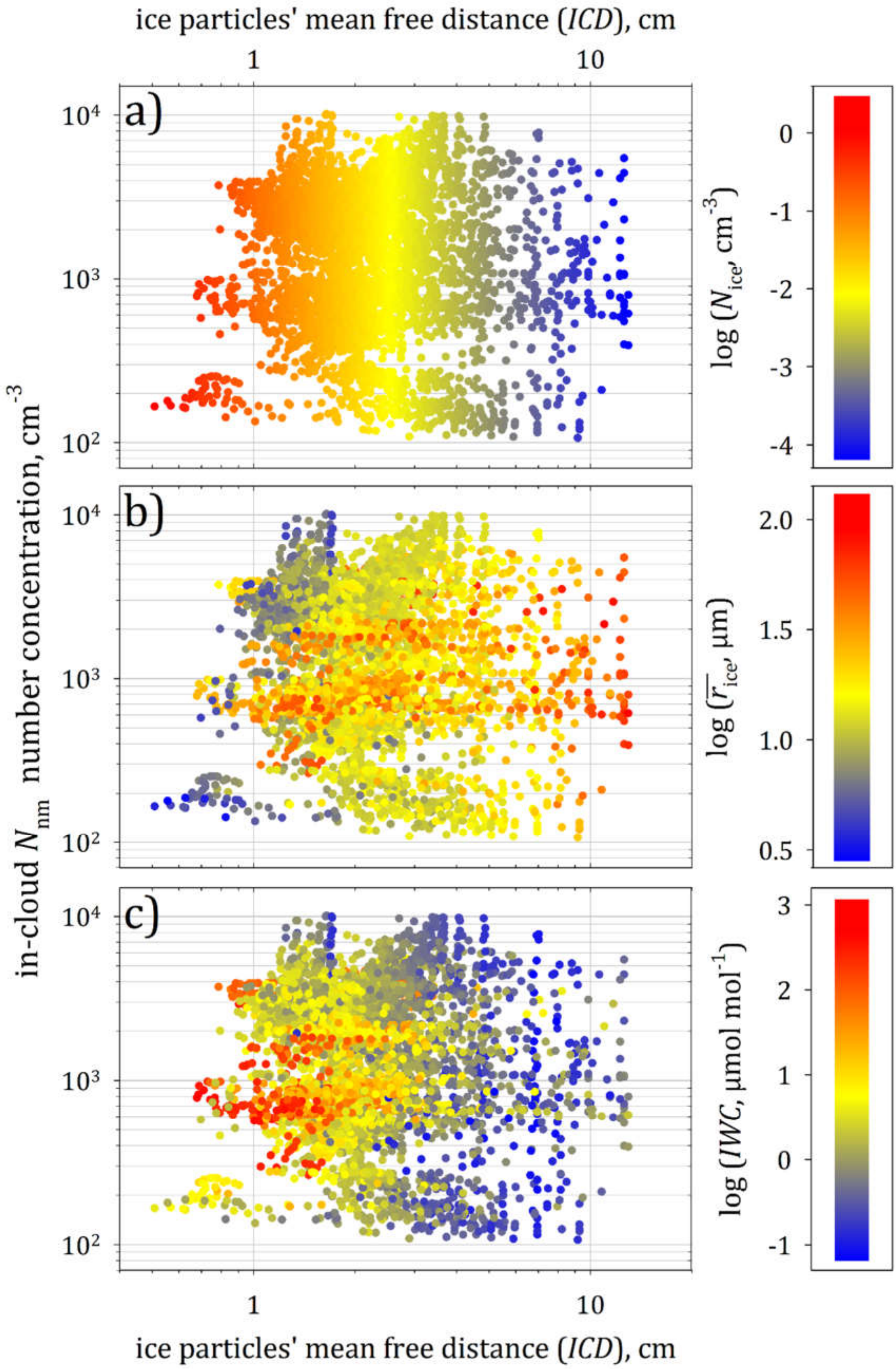
ice particles' mean free distance (ICD), cm
1
10
a)
b)
c)
10^4
10^3
10^2
in-cloud N_{nm} number concentration, cm^{-3}
log (N_{ice}, cm^{-3})
0
-1
-2
-3
-4
log ($\overline{r_{ice}}$, µm)
2.0
1.5
1.0
0.5
log (IWC, µmol mol^{-1})
3
2
1
0
-1
ice particles' mean free distance (ICD), cm

Figure 7

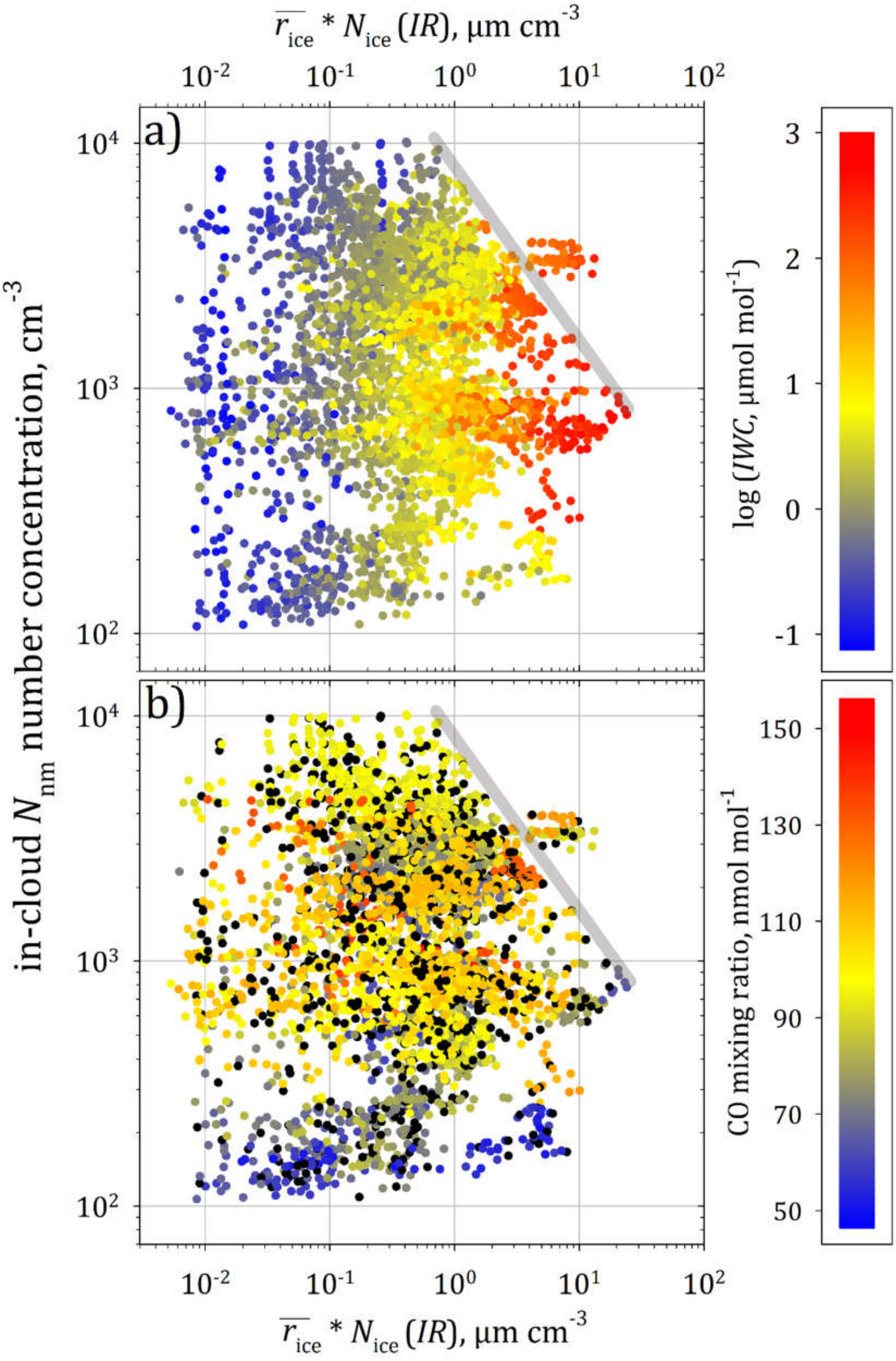

$\overline{r}_{\mathrm{ice}} * N_{\mathrm{ice}}$ (*IR*), μm cm^{-3}
10^{-2}
10^{-1}
10^{0}
10^{1}
10^{2}
a)
b)
10^{4}
10^{3}
10^{2}
in-cloud N_{nm} number concentration, cm^{-3}
log (*IWC*, μmol mol^{-1})
3
2
1
0
-1
CO mixing ratio, nmol mol^{-1}
150
130
110
90
70
50

Figure 8

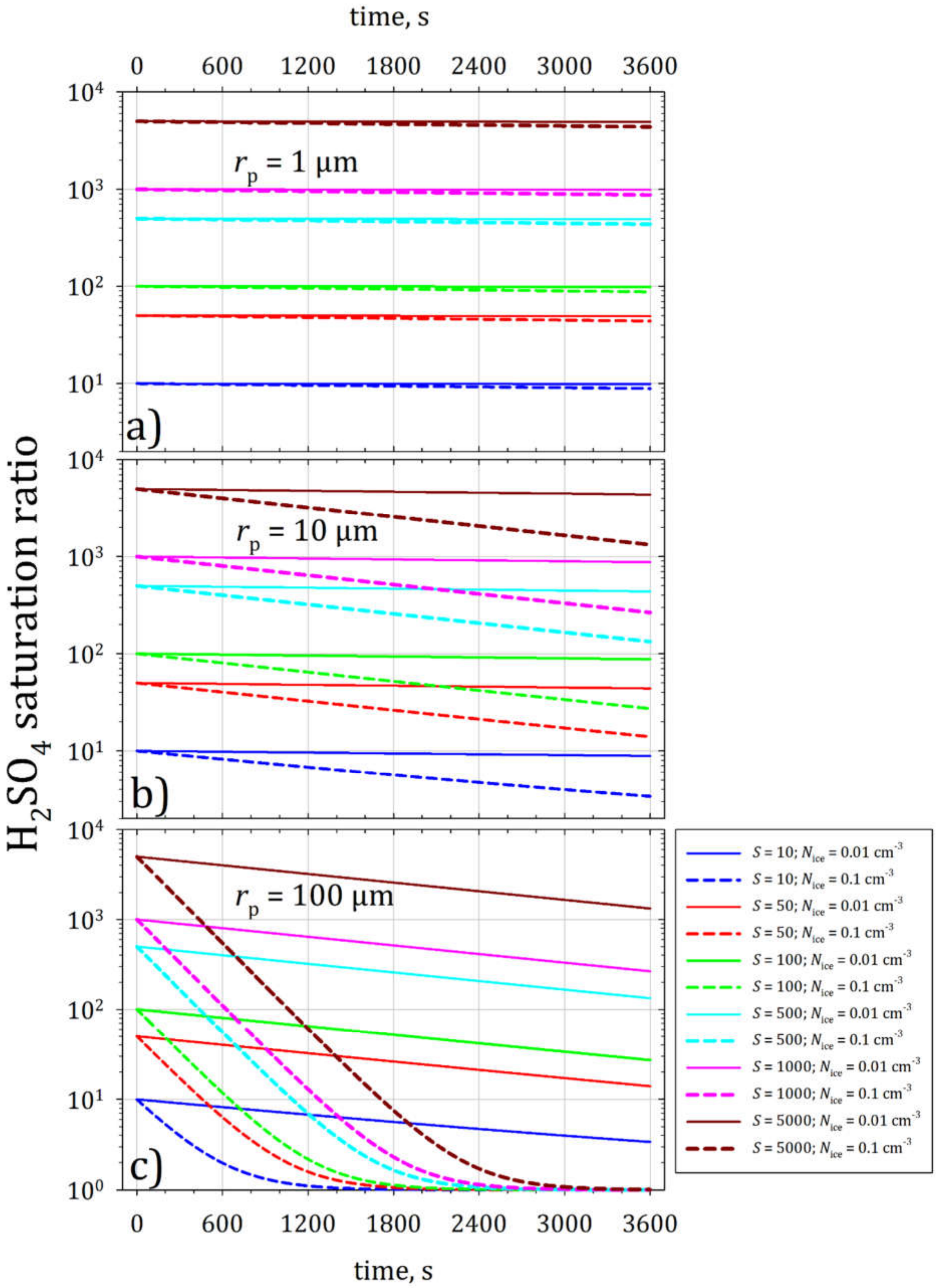
time, s
0
600
1200
1800
2400
3000
3600
10^4
10^3
10^2
10^1
r_p = 1 µm
a)
10^4
10^3
10^2
10^1
r_p = 10 µm
b)
10^4
10^3
10^2
10^1
10^0
r_p = 100 µm
c)
H_2SO_4 saturation ratio
S = 10; N_{ice} = 0.01 cm^{-3}
S = 10; N_{ice} = 0.1 cm^{-3}
S = 50; N_{ice} = 0.01 cm^{-3}
S = 50; N_{ice} = 0.1 cm^{-3}
S = 100; N_{ice} = 0.01 cm^{-3}
S = 100; N_{ice} = 0.1 cm^{-3}
S = 500; N_{ice} = 0.01 cm^{-3}
S = 500; N_{ice} = 0.1 cm^{-3}
S = 1000; N_{ice} = 0.01 cm^{-3}
S = 1000; N_{ice} = 0.1 cm^{-3}
S = 5000; N_{ice} = 0.01 cm^{-3}
S = 5000; N_{ice} = 0.1 cm^{-3}
0
600
1200
1800
2400
3000
3600
time, s

Figure B- 1

Table 1: NPF data set of StratoClim 2017, separated by event detection under clear-air (i.e. $N_{\mathrm{ice}} = 0\ \mathrm{cm}^{-3}$) and in-cloud conditions (i.e. $N_{\mathrm{ice}} > 0\ \mathrm{cm}^{-3}$). Discussed in-cloud NPF events (104 incidents that comply with introduced NPF criterion, Section 2.2) are partially embedded in larger clear-air NPF fields with continuously elevated N_{nm}. The total number of measurement seconds with NPF detections under either of both conditions is scaled to the total data set of the CN measurements and the total duration of NPF encounters. The mean horizontal distance is calculated from the event duration based on a mean flight speed of the M-55 *Geophysica* (154 ± 39 m s^{-1}) providing an equivalent horizontal extension of NPF. Geometric heights are interpolated values with maximum range of scattering from UCSE data of the eight flights.

NPF condition	total duration seconds	total duration hh : mm	percentage of NPF data	percentage of total dataset	mean horizontal distance in km
clear-air	4866	01 : 21	~ 51.2 %	~ 5.3 %	~ 750
in-cloud	4634	01 : 17	~ 48.8 %	~ 5.0 %	~ 714

in-cloud NPF

potential temperature	geometric altitude	total duration seconds	total duration hh : mm	percentage of in-cloud NPF	mean horizontal distance in km
355 – 360 K	~ 11 ± 2.5 km	432	00 : 07	~ 9.3 %	~ 67
360 – 365 K	~ 13.5 ± 2 km	1231	00 : 21	~ 26.6 %	~ 190
365 – 370 K	~ 15.3 ± 1 km	1455	00 : 24	~ 31.4 %	~ 224
370 – 375 K	~ 15.8 ± 1 km	1375	00 : 23	~ 29.7 %	~ 212
> 375 K	$\gtrsim$ 16.0 km	141	00 : 02	~ 3 %	~ 22